

**NAVAL POSTGRADUATE SCHOOL
Monterey, California**



THESIS

**AEROSOL OPTICAL DEPTH RETRIEVAL BY NPS MODEL
MODIFIED FOR SEAWIFS INPUT**

by

Brady A. Brown

March 2002

Thesis Advisor: Philip A. Durkee
Co-Advisor: Kenneth L. Davidson

Approved for public release, distribution is unlimited.

Report Documentation Page

Report Date 29 Mar 2002	Report Type N/A	Dates Covered (from... to) - -
Title and Subtitle Aerosol Optical Depth Retrieval by NPS Model Modified for SEAWIFS Input		Contract Number
		Grant Number
		Program Element Number
Author(s) Brown, Brady		Project Number
		Task Number
		Work Unit Number
Performing Organization Name(s) and Address(es) Naval Postgraduate School Monterey, California		Performing Organization Report Number
Sponsoring/Monitoring Agency Name(s) and Address(es)		Sponsor/Monitor's Acronym(s)
		Sponsor/Monitor's Report Number(s)
Distribution/Availability Statement Approved for public release, distribution unlimited		
Supplementary Notes The original document contains color images.		
Abstract		
Subject Terms		
Report Classification unclassified		Classification of this page unclassified
Classification of Abstract unclassified		Limitation of Abstract UU
Number of Pages 77		

THIS PAGE INTENTIONALLY LEFT BLANK

REPORT DOCUMENTATION PAGE

Form Approved OMB No.
0704-0188

Public reporting burden for this collection of information is estimated to average 1 hour per response, including the time for reviewing instruction, searching existing data sources, gathering and maintaining the data needed, and completing and reviewing the collection of information. Send comments regarding this burden estimate or any other aspect of this collection of information, including suggestions for reducing this burden, to Washington headquarters Services, Directorate for Information Operations and Reports, 1215 Jefferson Davis Highway, Suite 1204, Arlington, VA 22202-4302, and to the Office of Management and Budget, Paperwork Reduction Project (0704-0188) Washington DC 20503.

1. AGENCY USE ONLY (Leave blank)		2. REPORT DATE March 2002	3. REPORT TYPE AND DATES COVERED Master's Thesis
4. TITLE AND SUBTITLE Aerosol Optical Depth Retrieval By NPS Model Modified For SeaWiFS Input		5. FUNDING NUMBERS	
6. AUTHOR(S) Brady A. Brown		8. PERFORMING ORGANIZATION REPORT NUMBER	
7. PERFORMING ORGANIZATION NAME(S) AND ADDRESS(ES) Naval Postgraduate School Monterey, CA 93943-5000		10. SPONSORING/MONITORING AGENCY REPORT NUMBER	
9. SPONSORING / MONITORING AGENCY NAME(S) AND ADDRESS(ES) N/A			
11. SUPPLEMENTARY NOTES The views expressed in this thesis are those of the author and do not reflect the official policy or position of the U.S. Department of Defense or the U.S. Government.			
12a. DISTRIBUTION / AVAILABILITY STATEMENT Approved for public release, distribution is unlimited.		12b. DISTRIBUTION CODE A	
13. ABSTRACT (maximum 200 words) Using visible wavelength radiance data obtained from the spaceborne Sea-viewing Wide Field-of-view Sensor (SeaWiFS), during the Aerosol Characterization Experiment-Asia (ACE-Asia), an analysis of aerosol optical depth (AOD) was completed by modification to the NPS AOD Model previously compiled for NOAA geosynchronous- and polar-orbiting satellites. The objective of the analysis was to calibrate the linearized, single-scatter algorithm, estimated bi-directional surface reflectance, and phase function parameters. The intent of the study was to provide enhanced temporal AOD coverage with the addition of the orbiting SeaWiFS eight-channel radiometer to the established NOAA constellation of five-channel AVHRR-equipped satellites. The work has operational significance in providing timely, accurate remote information to military operators of identification and targeting systems. Possible applications include detection and warning of international treaty violation or reducing the adverse public health effects by weapons of mass destruction or pollution advection on global weather patterns.			
14. SUBJECT TERMS Sea-viewing Wide Field-of-view Sensor, SeaWiFS, aerosol optical depth, AOD, dust, ACE-ASIA, Sea of Japan, East China Sea, Yellow Sea.		15. NUMBER OF PAGES 77	
		16. PRICE CODE	
17. SECURITY CLASSIFICATION OF REPORT Unclassified	18. SECURITY CLASSIFICATION OF THIS PAGE Unclassified	19. SECURITY CLASSIFICATION OF ABSTRACT Unclassified	20. LIMITATION OF ABSTRACT UL

NSN 7540-01-280-5500

Standard Form 298 (Rev. 2-89)
Prescribed by ANSI Std. Z39-18

THIS PAGE INTENTIONALLY LEFT BLANK

Approved for public release, distribution is unlimited.

**AEROSOL OPTICAL DEPTH RETRIEVAL BY NPS MODEL MODIFIED FOR
SEAWIFS INPUT**

Brady A. Brown
Lieutenant, United States Navy
B.S., United States Naval Academy, 1995

Submitted in partial fulfillment of the
requirements for the degree of

MASTER OF SCIENCE IN METEOROLOGY AND PHYSICAL OCEANOGRAPHY

from the

NAVAL POSTGRADUATE SCHOOL
March 2002

Author:

Brady A. Brown

Approved by:

Philip A. Durkee, Thesis Advisor

Kenneth L. Davidson, Co-Advisor

Carlyle H. Wash , Chairman
Department of Meteorology

THIS PAGE INTENTIONALLY LEFT BLANK

ABSTRACT

Using visible wavelength radiance data obtained from the spaceborne Sea-viewing Wide Field-of-view Sensor (SeaWiFS) during the Aerosol Characterization Experiment-Asia (ACE-Asia), an analysis of aerosol optical depth (AOD) was completed by modification to the NPS AOD Model. Cloud-free AOD estimates have been compiled in previous years from NOAA geosynchronous- and polar-orbiting satellite data and validated using surface sunphotometers. The objective of this thesis was to calibrate the linearized, single-scatter algorithm using estimated bi-directional surface reflectance and size-dependent phase function parameters. The intent of the study was to provide enhanced temporal AOD coverage in the littoral and open ocean environment with the addition of the orbiting SeaWiFS eight-channel radiometer to the established NOAA constellation of five-channel AVHRR-equipped satellites. Comparison to Aeronet ground stations provides *in-situ* ground truth. "Clean" ACE-Asia sky regions have a mode at SeaWiFS AOD around 0.25, while "dirty" dust plumes had a mode at AOD near 2.0, tailing beyond 4.0. Initial SeaWiFS AODs were about 20% higher than AVHRR in clean subregions and up to 100% higher in dirty subregions. Refined ozone and Rayleigh scatter parameters have reduced SeaWiFS excess AOD by 6% to 12%. Red tide surface effects and multiple scatter atmospheric effects were present, complicating current assumptions.

The work has operational significance in providing more timely remote sensing data to military operators of electro-optical identification and targeting systems.

THIS PAGE INTENTIONALLY LEFT BLANK

TABLE OF CONTENTS

I.	INTRODUCTION.....	1
A.	CURRENT DETECTION OF AEROSOL	2
B.	IMPORTANCE OF AEROSOL DETECTION.....	4
II.	AEROSOL OPTICAL DEPTH RETRIEVAL	7
A.	RADIATIVE TRANSFER THEORY	7
B.	AN INVERSE SOLUTION TO THE RADIATIVE TRANSFER PROBLEM.....	10
1.	Aerosol Radiance	10
2.	Backscatter Parameterization.....	13
III.	EXPERIMENTAL DATA.....	17
A.	PURPOSE OF ACE-ASIA	17
B.	INSTRUMENTS.....	19
1.	NOAA AVHRR/3	19
2.	NASA SeaWiFS	20
3.	Aeronet Cimel CE 318-1	21
IV.	RESULTS	23
A.	IMAGERY RETRIEVAL AND PROCESSING.....	23
B.	NPS MODEL CODE PARAMETERIZATION.....	23
C.	CRITICAL EVENTS	24
1.	Similar AOD, Different Look Angle: Day 115..	27
a.	Weather at Nearest Aeronet Station	29
b.	NPS Model Output	30
2.	Similar Look Angle, Different AOD: Day 102..	33
a.	Weather at Nearest Aeronet Station	38
b.	NPS Model Output	39
3.	Extremely high AOD event: Day 100.....	42
a.	Weather at Nearest Aeronet Station	45
b.	NPS Model Output	46
D.	VALIDATION.....	47
V.	CONCLUSIONS & RECOMMENDATIONS	53
LIST OF REFERENCES.....	57	
INITIAL DISTRIBUTION LIST	61	

THIS PAGE INTENTIONALLY LEFT BLANK

LIST OF FIGURES

Figure 1.	NOAA-16 and AVHRR/3. (From: Brown)	2
Figure 2.	OrbView-2 and SeaWiFS. (From: Hooker)	3
Figure 3.	ACE-Asia Network and Cimel 318-1.....	4
Figure 4.	SeaWiFS channels over atmospheric windows.	8
Figure 5.	AVHRR channels over solar irradiance.....	8
Figure 6.	Radiometer radiance reception limited by channel width.....	9
Figure 7.	A summation of the NPS model treatment of the radiative transfer theory. (After: Durkee)	11
Figure 8.	Look-up table method for approximating phase function. (After: Durkee)	14
Figure 9.	Dust storm crossing the Pacific Ocean.....	18
Figure 10.	AVHRR spectral response (chs. 1 & 2).	19
Figure 11.	SeaWiFS bands six and eight.....	21
Figure 12.	"Typical" cloud patterns: GMS April 5, 2001.	26
Figure 13.	Prevailing spring conditions combined with: topographic effect, left; mesoscale wind pattern, right.....	26
Figure 14.	NOAA-16 pass 20011150433Z; April 25, 2001. . .	27
Figure 15.	SeaWiFS pass 20011150433Z; April 25, 2001. . .	28
Figure 16.	Meteorological conditions for April 15, 2001.....	29
Figure 17.	SeaWiFS AOD, NOAA-16 AOD, AOD difference, and GMS showing cloud cover for April 25, 2001. . .	30
Figure 18.	Percent difference between SeaWiFS and AVHRR AOD for April 25, 2001.	31
Figure 19.	Latest iteration of NPS AOD algorithm for April 25,.2001	32
Figure 20.	NOAA-16 pass 20011020508Z, April 12, 2001. . .	34
Figure 21.	SeaWiFS pass 20011020333ZZ; April 12, 2001. .	35
Figure 22.	Red tides in the Yellow Sea from the R/V <i>Ron H. Brown</i> . (Photo courtesy of Piotr Flatau)	36
Figure 23.	Red tides and coastal turbidity variation from space; April 12-14, 2001.....	37
Figure 24.	Meteorological conditions for April 12, 2001.....	38
Figure 25.	SeaWiFS AOD, NOAA-16 AOD, AOD difference, and Aeronet data for April 12, 2001.....	39
Figure 26.	Percent difference between SeaWiFS and AVHRR AOD for April 12, 2001.	40
Figure 27.	NOAA-16 AOD product, April 12, 2001.....	41

Figure 28. Latest iteration of NPS AOD algorithm for April 12,.2001	41
Figure 29. NOAA-16 pass 20011000349Z; April 10, 2001. . .	43
Figure 30. SeaWiFS pass 20011000345Z; April 10, 2001. . .	44
Figure 31. Meteorological conditions for April 10, 2001.....	45
Figure 32. SeaWiFS AOD 20011000345Z; April 10, 2001. . .	46
Figure 33. Initial summary of SeaWiFS and NOAA-16 AOD compared to Aeronet ground Observation at 870 nm, with linear best-fit superimposed.....	48
Figure 34. SeaWiFS AOD comparison with Aeronet ground observations at 670 nm.	49
Figure 35. SeaWiFS AOD comparison with Aeronet ground observations at 870 nm.	50

LIST OF TABLES

Table 1. Corrected parameterization for NPS SeaWiFS AOD algorithm.....	47
Table 2. Reduction in SeaWiFS AOD error with improved parameterization.	51

THIS PAGE INTENTIONALLY LEFT BLANK

ACKNOWLEDGEMENTS

I would like to thank Dr. Philip A. Durkee for his guidance and patience while instructing me on this topic. It would have been impossible to complete the data analysis portion of this project without the tireless efforts of Kurt Nielsen of the NPS Remote Sensing Lab. Finally, I would like to remember LCDR James Rocha for raising my spirits and allowing me to manage the many obstacles of late by his example and words of encouragement.

The author would like to thank the SeaWiFS Project (Code 970.2) and the Goddard Earth Sciences Data and Information Services Center/Distributed Active Archive Center (Code 902) at the Goddard Space Flight Center, Greenbelt, MD 20771, for the production and distribution of these data, respectively. These activities are sponsored by NASA's Earth Science Enterprise.

THIS PAGE INTENTIONALLY LEFT BLANK

I. INTRODUCTION

Satellite imagery from the National Oceanographic and Atmospheric Administration (NOAA) -16 and Orbview-2 polar-orbiters are used to estimate aerosol optical depth. In this thesis, an experiment over east Asia combines the untested SeaWiFS sensor algorithm with ground station observations and the well-calibrated AVHRR/3 algorithm. A first iteration of corrections to the SeaWiFS product are completed, and a discussion of the changing weather conditions and variables involved in this process follow.

Crude aerosol detection from space began with the first successful Suomi radiometer images from Explorer 7, launched on October 13, 1959. Similar direct observations of agricultural burning, desert dust storms, and volcanic eruptions are made to this day. Slightly more advanced limb scattering measurements for diffuse stratospheric particles were first hand-made by Apollo-Soyuz astronauts in 1975, and the initial tropospheric estimates were made using ERTS-1 (Landsat) the same year.

While precision has improved and spatial resolution has increased, temporal overhead frequency of aerosol observations is still limited by overhead coverage. Geostationary satellites provide whole-disc coverage every half-hour at the expense of resolution from higher altitude orbits. Sun-synchronous polar-orbiters are cheaper to launch and thus carry the latest, highest-quality instruments. Their low-earth orbit profile does limit them to only view about half the earth twice daily and sometimes have gaps in their coverage.

A. CURRENT DETECTION OF AEROSOL

Directly sampling the constituents of the atmosphere, including aerosols, would require climbing the tops of mountains, launching balloons, or flying instrumented airplanes to detect aerosol particles. We use remote sensing to gain timely, global, and relatively inexpensive observational coverage.

NOAA's newest polar-orbiter, N-16, (Figure 1) went into orbit in September, 2000 carrying the Advanced Very High Resolution Radiometer (AVHRR/3). It is capable of 1.09 km resolution in five channels, two broad wavelength bands of which are partly in the visible light spectra. She orbits at 870 km above earth in a 98.7° retrograde orbit, passing the equator northward (ascending node) at 1:40 PM. Her precession of 0.986° per day keeps the sun at a constant angle in the west on her afternoon passes. The AVHRR views $\pm 55.3^\circ$ from nadir for a swath width of 2,400 km. About a third of the swath is affected by sunglint to varying degrees depending on latitude and wind speed. Storms causing large wave heights increase the sunglint extent due to reflection off individual crest facets.

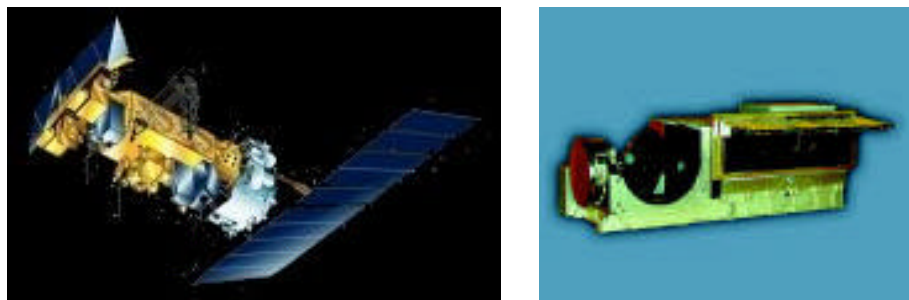


Figure 1.

NOAA-16 and AVHRR/3. (From: Brown)

Orbital Imaging Corporation's OrbView-2 (Figure 2) was launched in August, 1997 carrying the Sea-viewing Wide Field-of-view Sensor (SeaWiFS). Its eight narrow visible-spectrum wave bands provide 1.13 km resolution from a noon ascending node 705 km above the earth. It sees a swath 2,801 km wide by sweeping $\pm 58.3^\circ$ over a point $\pm 20^\circ$ off nadir, thus avoiding sunglint.

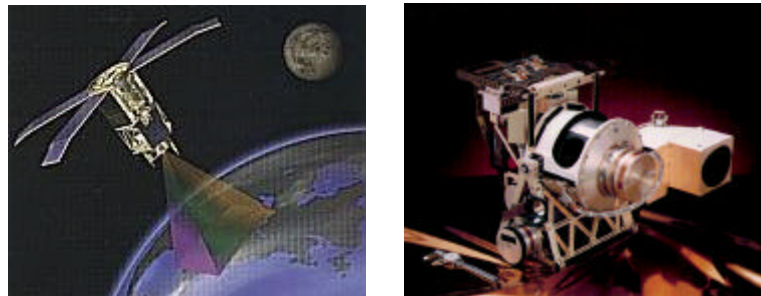


Figure 2. OrbView-2 and SeaWiFS. (From: Hooker)

These space sensors must be calibrated to ground truth to assure accuracy. Local measurements are made under a variety of conditions - marine, desert, forest, or mountainous terrain - depending on the remote sensing objective. For ACE-Asia, the AERONET program deployed a network of sunphotometers shown in Figure 3 from the Gobi Desert at the foothills of the Himalayan Mountains eastward to islands in the western Pacific Ocean. More details of these sensors will be discussed in Chapter III.

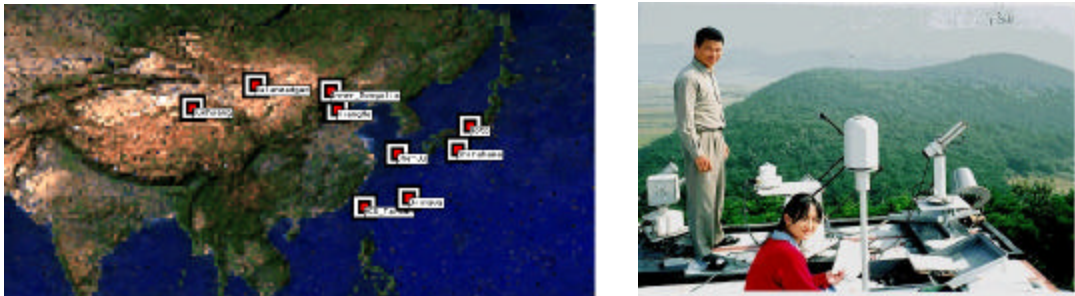


Figure 3.

ACE-Asia Network and Cimel 318-1.
(From: Bates et.al.)

B. IMPORTANCE OF AEROSOL DETECTION

Aerosols, in addition to causing health and pollution concerns, act indirectly to counter the "greenhouse" warming effect by increasing reflected solar energy back to space. Though tiny, individual particles scatter light according to their size, shape, and chemical composition. From high overhead, the satellite measures solar radiation scattered out of the atmosphere. The ocean appears dark, while aerosols are a spatially and temporally variable source of scattered radiance. Aerosol particles are kicked up by high winds or lofted from anthropogenic and natural sources, carried across thousands of miles by atmospheric currents, and ultimately fall out of the air column in precipitation and dry deposition processes. While thick smoke and pollution appears dark in color imagery, sea salts and haze brighten images by increasing backscatter towards the sensor much like a thin cirrus layer.

Military and private-sector interests alike are more reliant than ever on remote sensing and optical systems for weaponry, communications, safety, and logistics. A precise

knowledge of the aerosol conditions over foreign shores and above our own heads is critical for saving lives and increasing efficiency. The results of this experiment might have lasting effects on littoral optical forecasts for the warfighter and search-and-rescue personnel, or for treaty enforcement between governments.

THIS PAGE INTENTIONALLY LEFT BLANK

II. AEROSOL OPTICAL DEPTH RETRIEVAL

A. RADIATIVE TRANSFER THEORY

Energy reaching a satellite's radiometer comes from solar reflection or terrestrial emission. Sunlight enters the earth's atmosphere and scatters back to space or reflects off the planet's surface. At longer wavelengths, infrared and microwave emission from the ground and atmospheric constituents are important, but emission is not important in the visible region. The reflected intensity changes due to scatter into or out of the beam as well as loss along the path due to absorption. Little sunlight is reflected from the ocean surface except in a narrow sunglint region defined by the geometry required for specular (mirror-like) reflection. Like the greater reflection from clouds and land surfaces, the small diffuse portion of ocean surface reflectance increases the expected brightness level received at the sensor beyond what would be expected from the gaseous atmosphere alone. A further increase can come from diffuse multiple-scattering from just below the ocean surface, when light interacts with suspended particles in the water column. As will be discussed further, this complicates littoral minehunting operations when turbid outflow or plankton blooms are present. These types of events are common along the Asian coast, giving the Yellow Sea its name.

Figure 4 indicates with colored bands the eight SeaWiFS channels plotted over portions of the atmosphere which allow high energy transmittance. These channels in the visible portion of the spectrum are: 0.402-0.422,

0.433-0.453, 0.480-0.500, 0.500-0.520, 0.545-0.565, and 0.660-0.680 μm . In the near-infrared, SeaWiFS measures wider bandwidths at 0.745-0.785 μm and 0.845-0.885 μm .

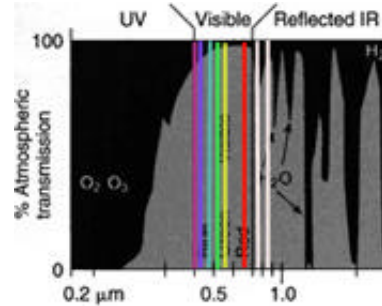


Figure 4. SeaWiFS channels over atmospheric windows.

Of particular interest are SeaWiFS channels six (0.670 μm) and eight (0.865 μm), shown in Figure 5, which correspond roughly to AVHRR channels one (0.580-0.680 μm , a lower frequency and five times wider bandwidth) and channel two (0.725-1.100 μm , nearly equal center wavelength but nearly 100 times wider bandwidth).

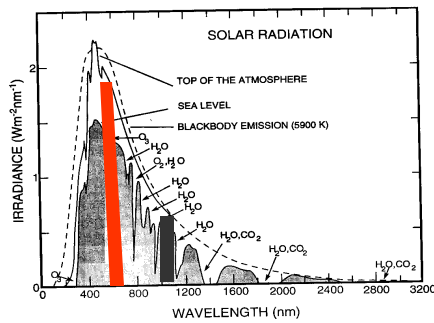


Figure 5. AVHRR channels over solar irradiance.

Band differences cause sensors to receive different amounts of reflected solar radiation, as shown by the representative areas under a theoretical Plank curve in Figure 6.

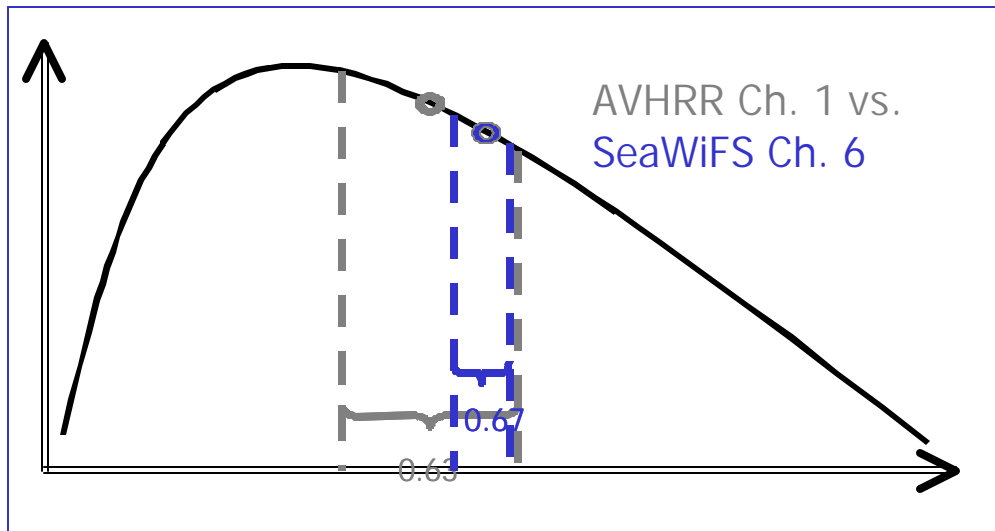


Figure 6. Radiometer radiancereception limited by channel width.

Particle size plays an important factor in light interaction as well. Light at increasing wavelengths interacts with particles of increasing size in one of three regimes. A size parameter is defined as particle diameter divided by wavelength ($c = 2\pi r / \lambda$). Scatter from cloud droplets and rain falls into the largest visible wavelength size parameter category, geometric optical scatter. This effect explains the common occurrence of rainbows and sky halos. Atmospheric molecules and tiny Aitken particles cause the smallest size parameter category, Rayleigh scatter. In between lies the Mie scatter regime in which dust and smoke particle size is roughly equal to the

wavelength of the visible light. This also explains why electromagnetic radiation at longer wavelengths, such as the upper infrared, microwave, and radar regions, have little interaction with aerosols.

This thesis assumes sunglint-free, cloud-free, clear water conditions and spherical aerosol particles. Constant surface reflection from sea foam caused by high winds and phytoplankton blooms is ignored. Correction factors for Rayleigh scatter and absorption due to ozone and water vapor are applied.

B. AN INVERSE SOLUTION TO THE RADIATIVE TRANSFER PROBLEM

Aerosol optical depth can be retrieved through an inverse process if the total measured radiance (L_t) is compared to the known solar constant (E_o).

1. Aerosol Radiance

Total extinction is the sum of absorption and scattering ($\mathbf{S}_e = \mathbf{S}_a + \mathbf{S}_s$) depending on wavelength. Radiance decreases proportional to the original intensity along the path according to Beer's law:

$$L(\mathbf{I}) = L_o e^{-\int \mathbf{S}(\mathbf{I}) dz} \quad (1)$$

Optical depth, then, is the integrated extinction coefficient for all wavelengths along the path:

$$\mathbf{d}(\mathbf{l}, z) = \int_0^{\infty} \mathbf{s}_s dz \quad (2)$$

The summation of radiation received by the satellite is shown in Figure 7 as the aerosol backscatter of interest (not shown), the Rayleigh molecular scatter (not that of light from the surface scattering into the sensor's field of view), and the percentage of surface reflected light and sunglint that the atmospheric transmissivity allows to pass through.

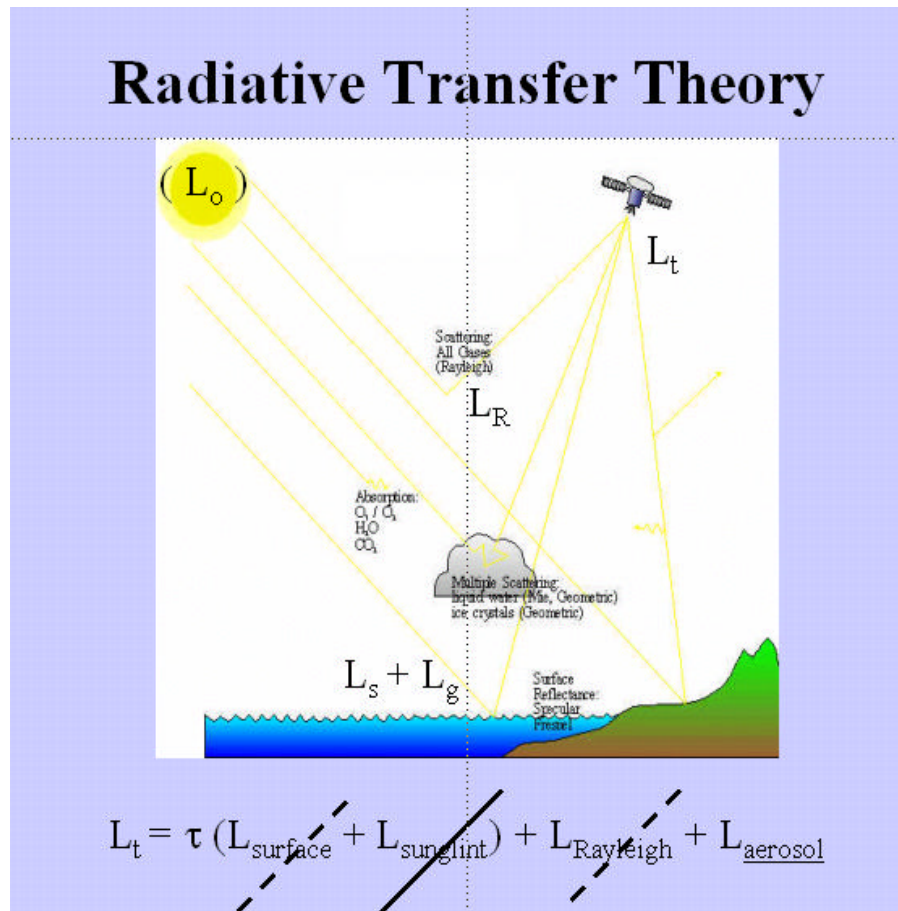


Figure 7. A summation of the NPS model treatment of the radiative transfer theory. (After: Durkee)

Liou (1980) gave the general form of total radiance through the atmospheric plane as:

$$\mathbf{m} \frac{dL_t(\mathbf{I}, \Omega)}{d\mathbf{d}} = L_t(\mathbf{I}, \Omega) - \frac{\mathbf{w}_o}{4\mathbf{p}} \left(\int_{4\mathbf{p}} L_t(\mathbf{I}, \Omega) p(\mathbf{y}_s) d\Omega + E_o \mathbf{p} p(\mathbf{y}_s) e^{-\mathbf{d}/\mathbf{m}} \right) \quad (3)$$

where \mathbf{w}_o is the single-scatter albedo (ratio of scatter extinction to total extinction) and ignoring multiple reflections in clouds or undersea. $P(\psi_s)$ is the scatter phase function for the single scattering angle (ψ_s) between the incoming solar irradiance and the satellite.

Solving the first order, linear, ordinary differential equation for aerosol sources of airborne scatter only:

$$L_t = L_o e^{-\mathbf{d}(\mathbf{I})/\mathbf{m}} + \frac{\mathbf{w}_o(\mathbf{I}) p(\mathbf{y}_s, \mathbf{I})}{4\mathbf{p}} E_{sun} \frac{(1 - e^{-\mathbf{d}(\mathbf{I}, z)(1/\mathbf{m}_o + 1/\mathbf{m})})}{(1/\mathbf{m}_o + 1/\mathbf{m})} \quad (4)$$

as notated by Durkee et al. (1991). In this single-scatter limited condition, the total radiance received includes in the first term, surface reflected energy not scattered out of the path. The second term includes the percentage of light that has scattered back from the atmosphere and happens to go in the direction of the receiver without transmitting to the surface or being absorbed.

Simplified, if the aerosol optical depth is assumed to be much less than one, the aerosol radiance becomes:

$$L_{aerosol} = \frac{\mathbf{w}_o p(\mathbf{y}_s)}{4\mathbf{p}} E_{sun} \frac{\mathbf{d}}{\mathbf{m}} \quad (5)$$

from Kidder & Vonder Harr (1995). L_a is proportional to ω_0 , $p(\psi_s)$, and d_a , and the increased brightness measured from space is accounted for by the optical depth of the aerosol modified by the directionality of the scatter and the particle absorption.

2. Backscatter Parameterization

Backscatter towards the sensor is one of the keys to the inverse solution. The NPS model currently assumes only simple "single-scattering" of light off of spherical aerosol and back towards the satellite sensor. The amount of energy scattered and absorbed off an aerosol surface is determined by the index of refraction ($m = n + i n'$). In the visible and near-infrared portions of the spectrum, absorption is negligible. Scattering includes not only photons which strike a particle, but those which refract around while passing near it. Double integrals in the solution to Eq. (3), even neglecting irregular shapes, are difficult to estimate since knowledge of radiance into the scattering volume from all directions is required.

One way to get around this problem is the use of look-up tables for phase function values determined by a variety of aerosol types and size distributions. Since the scattering is determined by the product of the Mie scattering efficiency which peaks near particle radii equal to the wavelength, the more steeply the number of particles falls off as size increases, the greater the change in scattering as a function of wavelength. Figure 8 shows the process of determining an optical depth using the NPS model.

NPS Aerosol Model

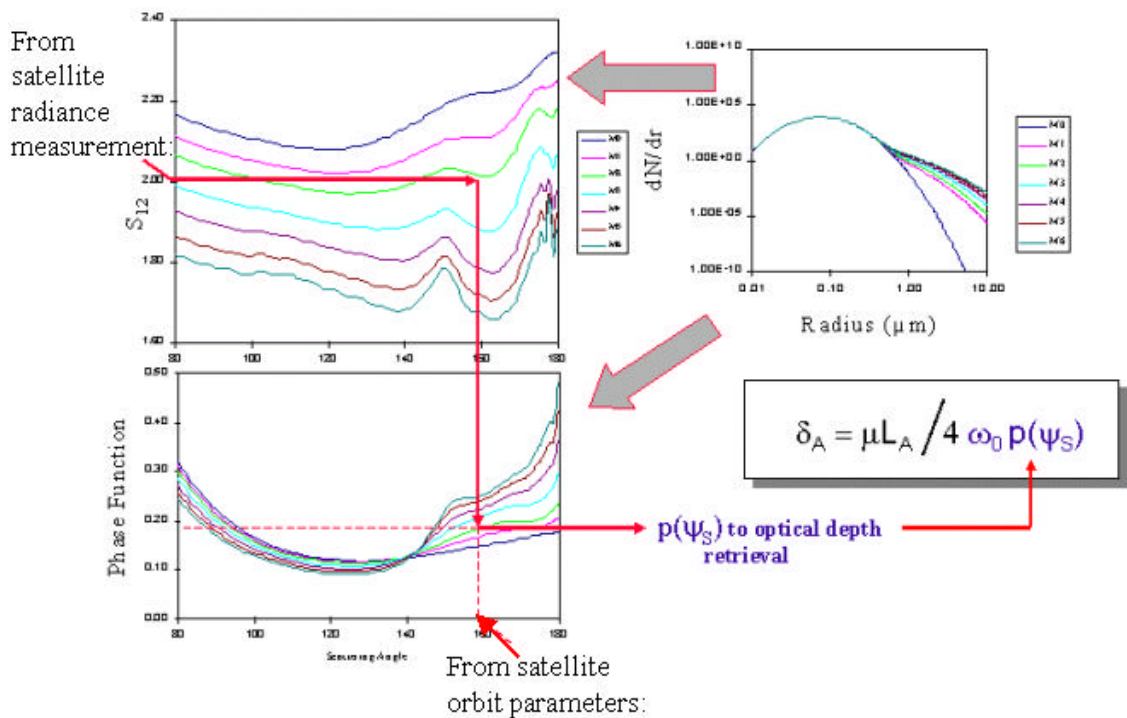


Figure 8.

Look-up table method for approximating phase function. (After: Durkee)

The ratio of AVHRR channels one and two (or SeaWiFS channels six and eight) determines the size distribution and phase function for the scatter angle determined by the satellite-solar geometry. This estimated phase function allows calculation of an aerosol optical depth:

$$\mathbf{d}_a = L_a \frac{1}{4\mathbf{p}} \frac{1}{p(\mathbf{y}_s)} \mathbf{m} \quad (6)$$

If a higher size distribution number is selected, the result is that the model assumes a larger percentage of small particles are present in the atmosphere. These smaller particles have the size parameter (χ) closer to unity. The increased phase function assumed by the model on the right side of the bottom-left plot would increase for values of scattering angle over 140° . Located in the denominator of Equation 6, the resulting aerosol optical depth calculation would be decreased. Conversely, at scattering angles less than 140° , an error in increased size distribution would decrease phase function and increase the output AOD.

A "two-stream Turner" routine accounts for ozone and Rayleigh scatter contributions to radiance measured at the receiver. A constant Rayleigh phase function formula of $\frac{3}{4}(1+\cos 2\psi_s)$ is used in this calculation. For a more detailed treatment of the multispectral parameterization routine used in the NPS model, see Brown, 98, pp. 24-27.

THIS PAGE INTENTIONALLY LEFT BLANK

III. EXPERIMENTAL DATA

A. PURPOSE OF ACE-ASIA

Global aerosol chemistry and transport measurements have been undertaken by the International Global Atmospheric Chemistry Program. Previous investigations have focused on ocean regions around Tasmania (ACE-I), the Canary Islands (ACE-II), the east coast of the United States (TARFOX), and the Indian Ocean (INDOEX). ACE-ASIA was held from March to May 2001 in order to quantify aerosol properties and their radiative effects over East Asia and the western North Pacific Ocean.

The winter Himalayan high drives northwest gales across the Gobi Desert. Tons of fine western desert mineral sand is joined by coal soot and SO₂ from the agricultural heart of China. Finally, the current picks up NO₂ emissions in the form of pollution from industrial factories and the auto traffic of crowded eastern Asian cities. Weather patterns carry these dirty air masses out over the Yellow Sea, the Sea of Japan, and several days later can even cross the Pacific to the west coast of the United States, as seen in Figure 9.

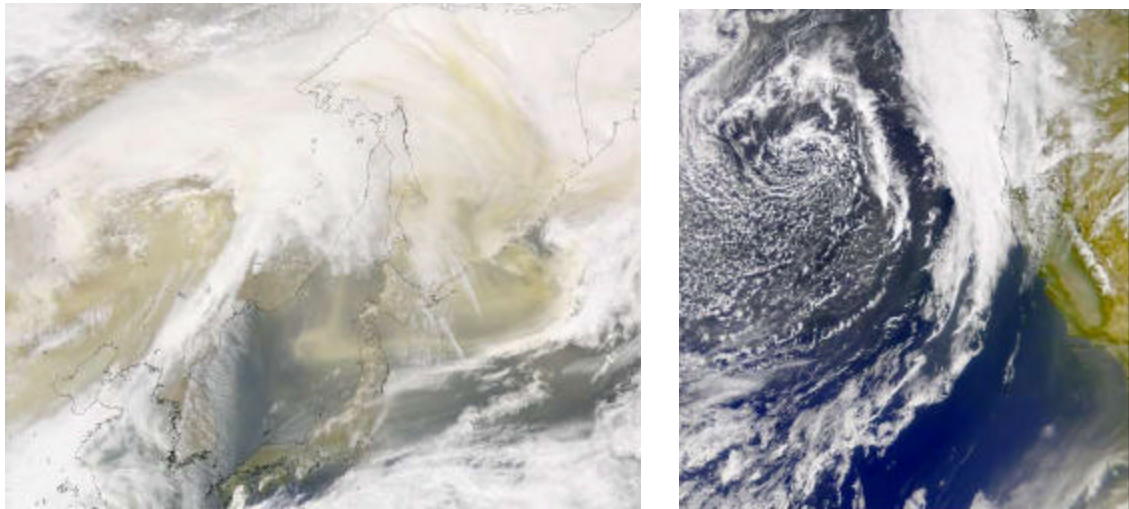


Figure 9. Dust storm crossing the Pacific Ocean.
Sea of Japan, 10 APR 01; Southern California, 16 APR 01.
(From: Hooker)

An unusual AOD observation of the ACE-ASIA experiment, besides the high AOD values, was the four-five day period of dust plumes following a frontal passage of the eastern Aeronet sites. Also, the western Aeronet sites experienced diurnal shifts from morning coal soot and industrial sulfates to afternoon and evening dust concentrations. Since this thesis includes only local afternoon overpasses, a mixture of the two particle types can be expected. Aerosol visible single-scatter albedo differences between African Saharan dust with sea-salt and nitrate mixes ($\omega_o = 0.8$ to 0.9 during ACE II by Collins, et. al.) and Asiatic Gobi Desert dust with industrial sulfate and coal soot mixes (from 0.3 to 0.95 by Xu and Bergin, 2001) have been reported. The effect of particle albedo in a visible light Mie scatter regime needs to be further investigated.

B. INSTRUMENTS

ACE-Asia joined scientific minds and resources from over ten countries. Terrestrial data collection was accomplished from land, sea, and air. In addition to the ground station radiometers and LIDARs, the R/V *Ronald H. Brown* and R/V *Murai* were involved, as well as aircraft including the NCAR C-130, NPS CIRPAS Twin Otter, and Australian King Air.

1. NOAA AVHRR/3

Channels one ($0.580 - 0.680 \mu\text{m}$) and two ($0.725 - 1.100 \mu\text{m}$) of the AVHRR/3 are used to estimate aerosol optical depth. A split-window cloud mask routine uses channels one, two, four ($10.3 - 11.3 \mu\text{m}$), and five ($11.5 - 12.5 \mu\text{m}$). The spectral response curves for channels one and two are shown in Figure 10.

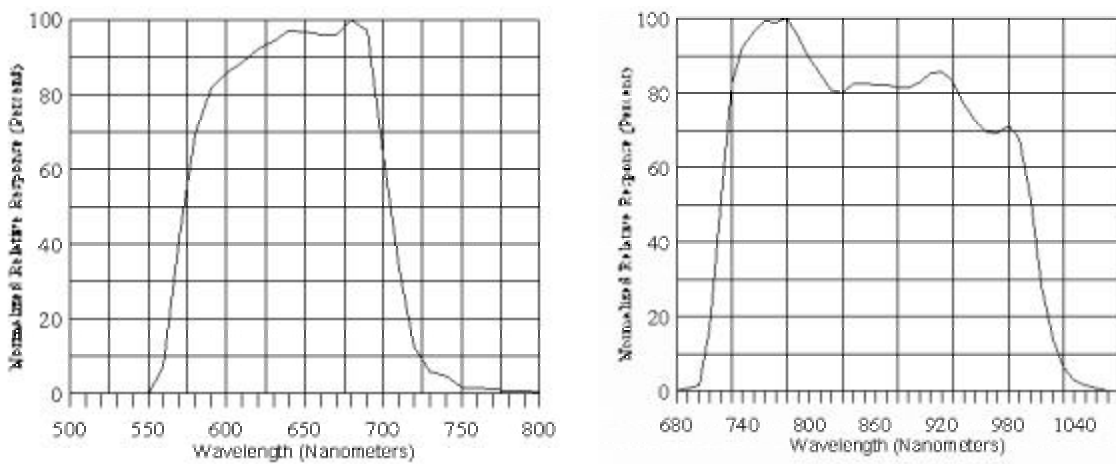


Figure 10.

AVHRR spectral response (chs. 1 & 2).

(From: Kidwell)

Experimental analysis yields an ozone absorption optical depth 0.027 in channel one and 0.0021 in channel two. The effects of Rayleigh scatter optical depths are assumed to be 0.057 in channel one and 0.019 in channel two.

2. NASA SeaWiFS

A successor to the Coastal Zone Color Scanner on NIMBUS-7, this multi-band color monitor can track meteorological events as well as detect subtle differences in biological activity in the world's oceans. Actually built and owned by Orbital Sciences Corporation, NASA buys and owns the right to all research data collected.

In order to extend coverage of bright areas without saturating the scanner, SeaWiFS uses discontinuous gain above 80% peak input. This bi-linear response allows, for example, channel one to detect upper tropospheric cloudtops, ice fields, or desert sands at up to $60.1 \text{ mW cm}^{-2} \mu\text{m}^{-1} \text{ sr}^{-1}$ vice the original limit of about $13.6 \text{ mW cm}^{-2} \mu\text{m}^{-1} \text{ sr}^{-1}$. The spectral response curves for SeaWiFS channels six and eight are shown in Figure 11 for comparison with AVHRR.

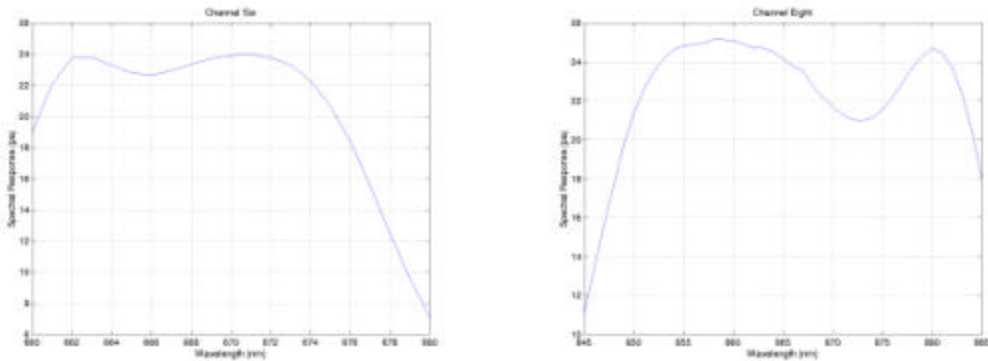


Figure 11. SeaWiFS bands six and eight.
(Author)

The ability of SeaWiFS to avoid sunglint by automated tilting is an advantage over AVHRR, but it can cause unusual streaks in SeaWiFS imagery as the tilt angle is changed.

3. Aeronet Cimel CE 318-1

The Aerosol Robotic Network (Aeronet) radiometer instrument detects transmitted solar intensity in five visible and three near-infrared channels (0.340 , 0.378 , 0.440 , 0.499 , 0.613 , 0.870 , 0.940 , and $1.020 \mu\text{m}$) . (ARM/NASA/DOE website, after Holben, 1997). AOD estimates are possible with an accuracy of ± 0.02 . Aerosol modal radius distribution information from 0.1 to $3 \mu\text{m}$ is estimated using a simple two-step radiative transfer algorithm which had not been fully validated as of June, 2001

Each unit uses a four-quadrant feedback system to center on the sun every fifteen minutes during daylight hours and sample incoming solar radiance using two

polarized collimator filters in front of the sensor. The original Aeronet sites in the continental United States are funded by the Department of Energy's Atmospheric Radiation Measurement program. These sensors have the ability to transmit their readings automatically over an uplink to a NOAA GOES relay. Nine remote, manned sites were combined with local data collection teams during ACE-Asia.

Data output screening is performed using a number of quality checks. First, samples are always taken in "triplets" separated by thirty seconds. Any sudden changes in AOD indicates cloud contamination. AODs less than 0.01 and very low sun angle measurements near twilight are thrown out to avoid the associated variability which would bias daily averages. Results greater than three standard deviations from the diurnal mean are discarded. However meticulous, these standards can allow thin, stable, uniform clouds to pass and misrepresent thick, quickly arising dust columns as cloud streaks.

IV. RESULTS

A. IMAGERY RETRIEVAL AND PROCESSING

Data collected during ACE-Asia and used in this study includes reference ground data sets, raw satellite radiance imagery, and supporting meteorological and oceanographic fields. The "ground truth" state of the atmosphere and underlying ocean are needed for accurate validation of aerosol optical depth retrievals. Ocean color variability affects aerosol measurements at the same time that aerosol changes affect water color data collection.

Preliminary data processing was accomplished with the Terascan software suite. For AVHRR and SeaWiFS images, the initial step was to build information on the swath from sun and satellite angles at each location being recorded. Precise spatial knowledge is required for image intercomparison. Radiance to reflectance conversion is applied based on wavelength dependence on E_o , day of year corrections for annual variation in incoming solar intensity, and satellite view geometry is used to georeference the image.

B. NPS MODEL CODE PARAMETERIZATION

Throughout the study, data quality was favored over quantity, and sections or entire passes were removed to minimize erroneous analysis. Sunglint removal was completed to remove anisotropic specular reflection into the receiver. Cloud screening was completed by a combination of automated and manual techniques. Due to the lack of infrared bandwidth receivers on SeaWiFS, a split-

channel method was partially ineffective. Previous AVHRR routines have compared cloudtop to surface temperatures, at the risk of confusing stratus and fog. Another method has been spatial coherence analysis to find cloudtop texture, though this might mistake thick aerosol or turbid sea surface filaments.

A visual analysis showed that patches of low closed-cell cumulus in the open ocean to the south and east of Japan often passed the automatic filter. Also, high turbidity from the Yangtze River carried into the western Yellow Sea renders composite AODs meaningless due to excessively high surface reflectance. Manual thresholds were required to remove bad pixels, even at the expense of some good data. In the end, average "clean" skies had AODs below about 0.25, "medium" periods had AODs up to 0.50, and "dirty" events had AODs as high as 4.0 and above. These extremes were corroborated by the AERONET ground stations. In comparison, on a hazy day over a large city on the east coast of the United States the AOD generally doesn't rise above about 0.5. All products included in this thesis have been limited to an AOD of 2.0 in order to show finer detail in weaker aerosol regions.

C. CRITICAL EVENTS

More than 120 SeaWiFS and NOAA-16 overpasses were downloaded during 45 days of ACE-ASIA operations. Imagery had to be selected to best represent the range of aerosol observed. This study required cloud-free passes which coincided in swath coverage and proximity to ground stations. Many swaths did not overlap with each other, and

often ground sites could not report readings due to local cloudiness that did not extend far across the coastline. Unfortunately, the same remote sites that were favorably far from industry and population centers frequently were affected by orographic clouds due to their hilltop locations. Twenty-seven matches were found between the sensors and these were narrowed to five choices that had the added benefit of closely matching overpass times, thereby avoiding advection of small aerosol features between images.

Two of these aerosol events have been selected to indicate the NPS AOD model performance under significantly different conditions. A third sample shows an extreme dust plume event. Prevailing conditions during the spring transition from winter to summer monsoon behavior are seen in Figures 12 & 13. During the 45-day experiment period, cloud patterns show frequent lows developing to the northeast of the Tibetan highlands, proceeding to sea over Korea and Japan. To the south and east of Japan the conditions are opposite: easterlies and surface highs form generally clear skies except for cumulus cells drifting from the vicinity of Okinawa towards Taiwan. Dust outbreaks generally follow these northern lows, trailing their associated cold fronts toward the southwest.

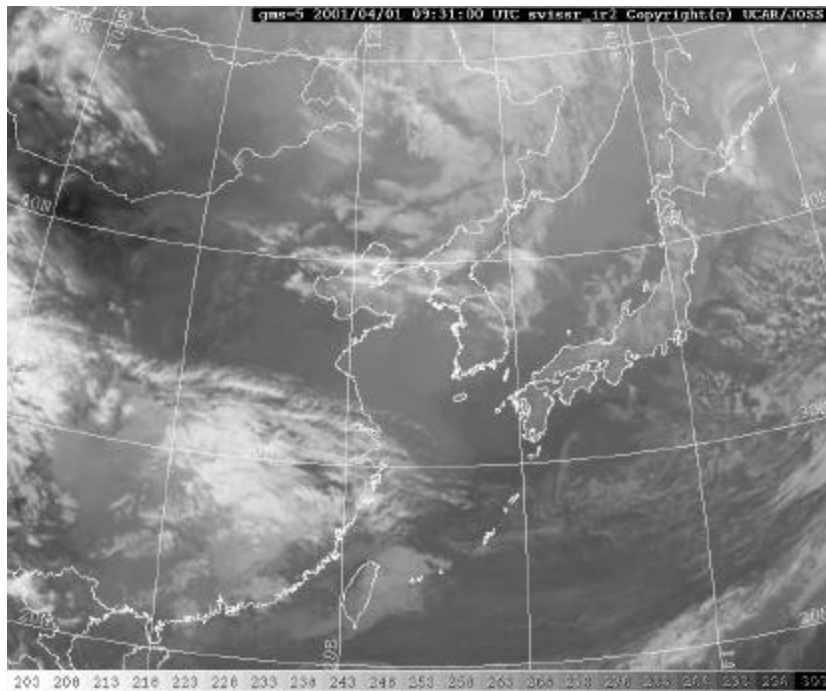


Figure 12. "Typical" cloud patterns: GMS April 5, 2001.

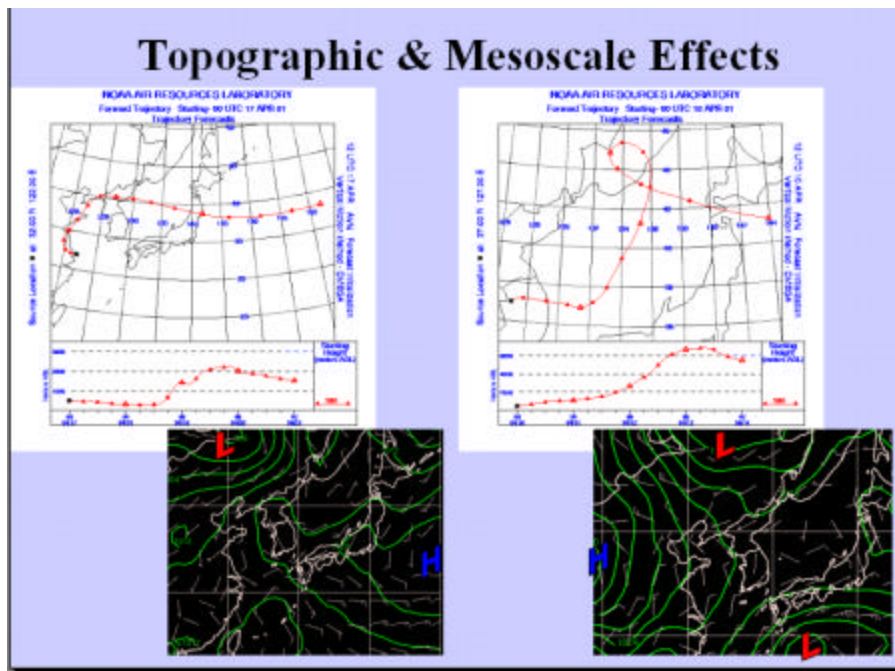


Figure 13. Prevailing spring conditions combined with:
topographic effect, left; mesoscale wind pattern, right.

1. Similar AOD, Different Look Angle: Day 115.

The first day selected shows similar AOD values and the effect of increased column distance on remote sensing. The location of interest for this case is $37^{\circ} 37'$ North latitude, $136^{\circ} 36'$ East longitude. On Figures 14 and 15, the point chosen for comparison is signified by the red star. The scattering angle is 128° on the SeaWiFS pass, while NOAA-16 has a scattering angle of 157°

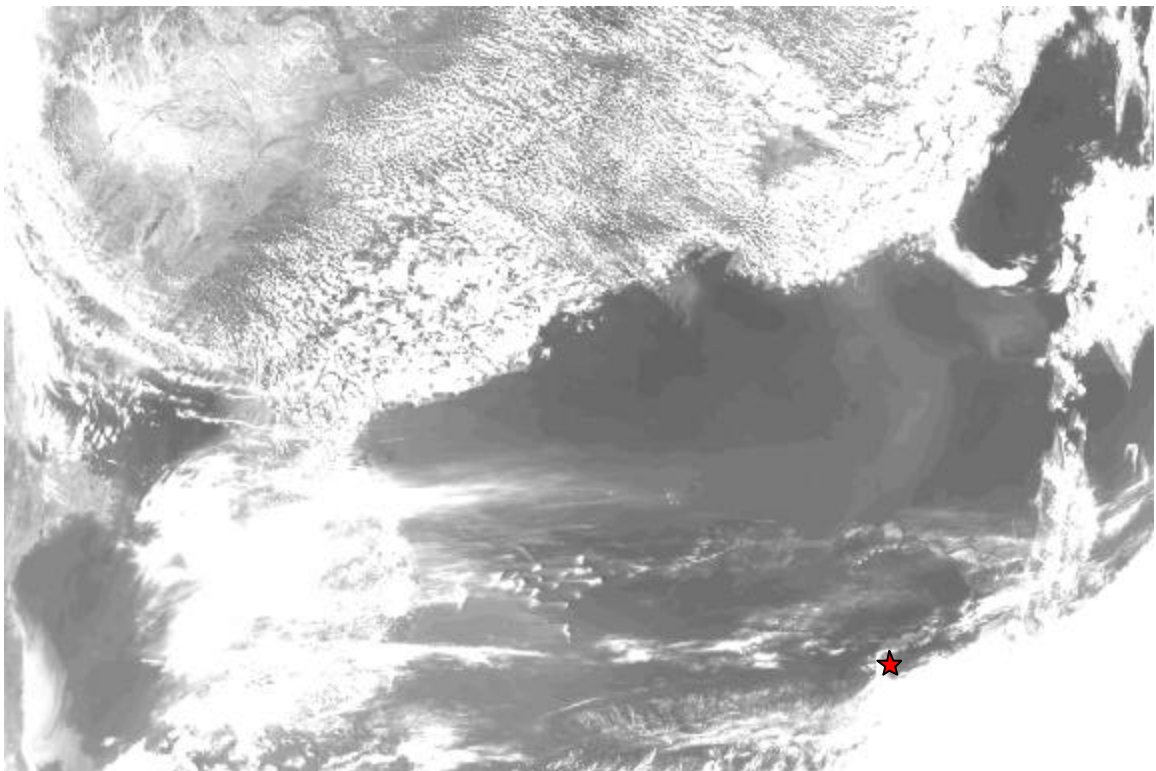


Figure 14.

NOAA-16 pass 20011150433Z; April 25, 2001.

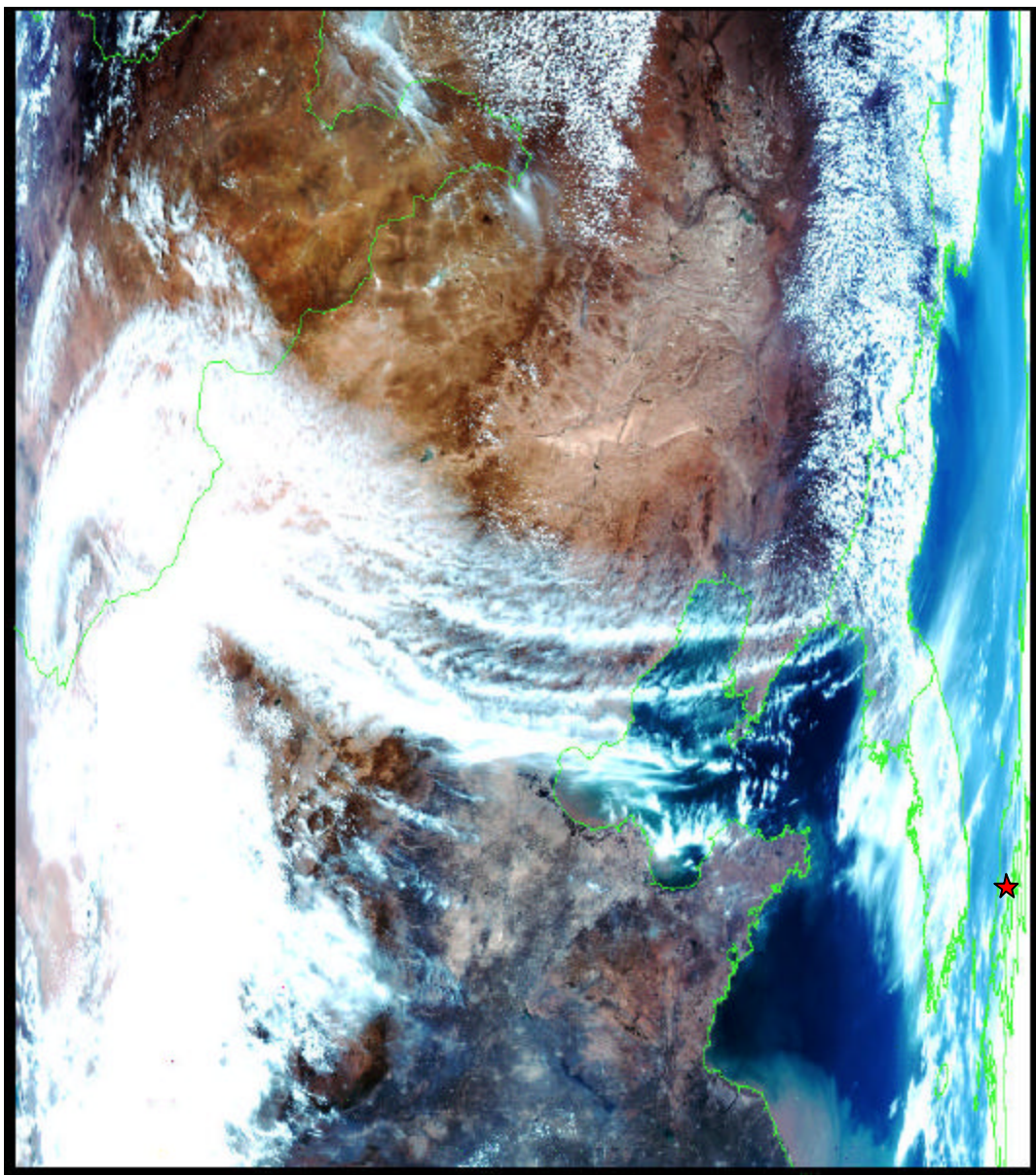


Figure 15.

SeaWiFS pass 20011150433Z; April 25, 2001.

a. Weather at Nearest Aeronet Station

Surface NOGAPS fields for case one are shown in Figure 16.

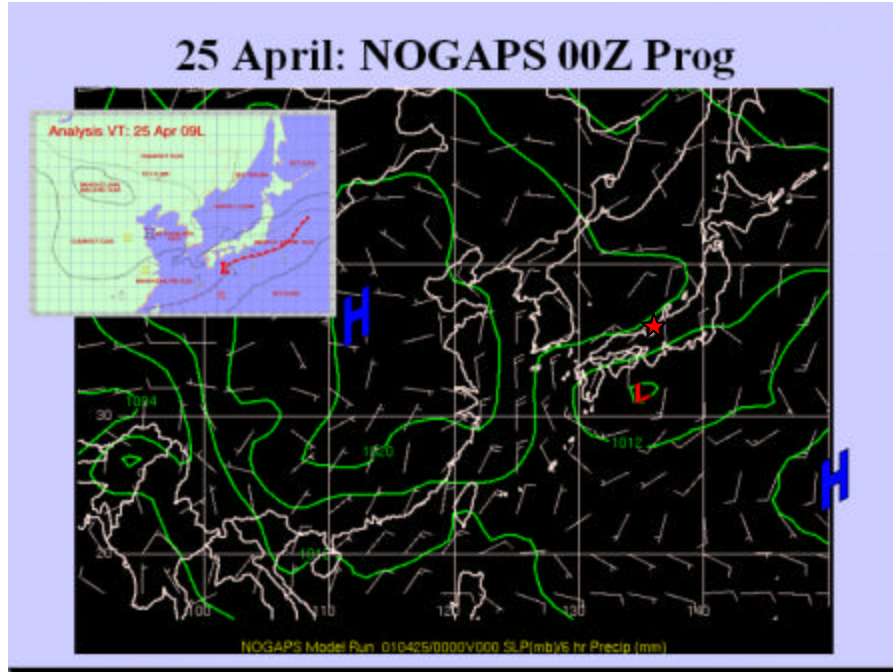


Figure 16. Meteorological conditions for April 15, 2001.

Unfortunately, although weather conditions had been calm for several previous days, only Noto, Japan had AERONET data nearby. This distance from Noto to the swath overlap was at least 375 kilometers, upwind, and so comparison between the two are marginally useful. Noto values peak at 0.28, about 25% lower than either satellite. Travel at the rate of this wind speed would take more than 72 hours. This is obviously too long for steady-state air advection.

b. NPS Model Output

Aerosol optical depth output for SeaWiFS and AVHRR are in the top row of Figure 17. On the bottom left is the difference between the two, and on the bottom right is a corresponding GMS image showing regions masked by cloud.

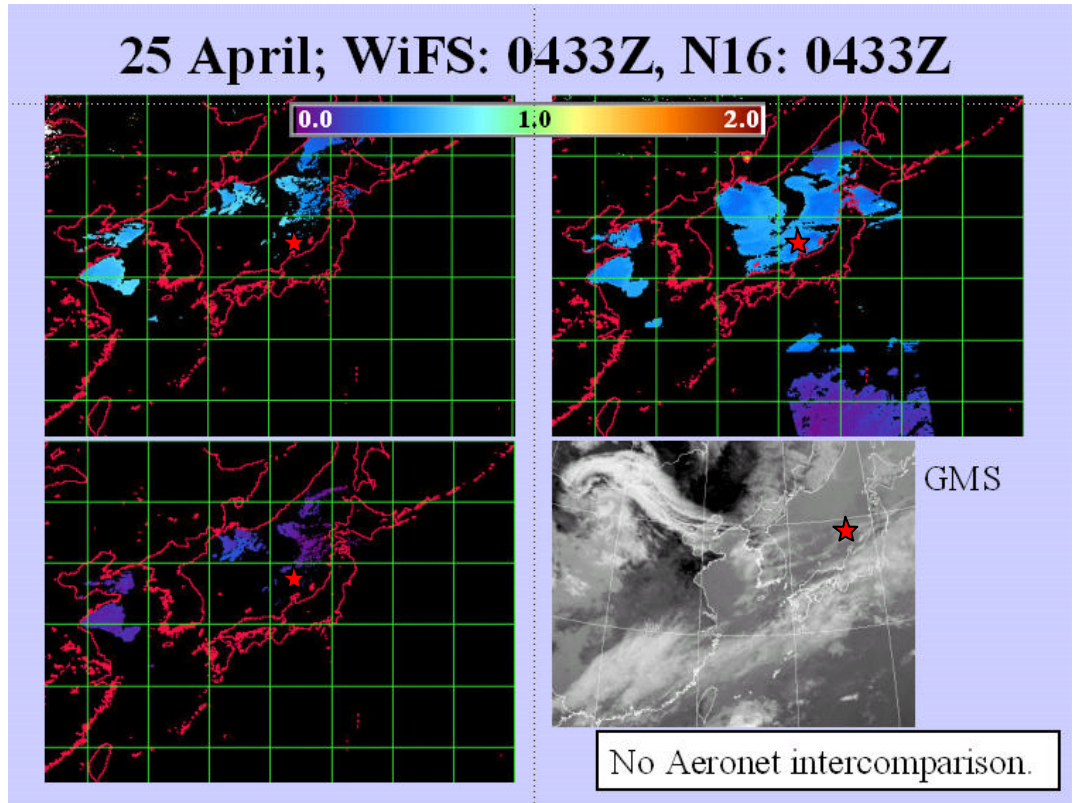


Figure 17.

SeaWiFS AOD, NOAA-16 AOD, AOD difference, and GMS showing cloud cover for April 25, 2001.

This set of AVHRR and SeaWiFS passes are unique for the study in that they have exactly the same overpass time. Generally low AOD values in light blue on the top two images are observed over the eastern Sea of Japan. Initial SeaWiFS parameterization coefficients produced an AOD value (top left plot) of 0.50; improvements to ozone

and Rayleigh scatter parameterization brought this down to 0.46, a decrease of 8.0%. The AVHRR optical depth value (top right plot) of 0.44 was 4.5% lower still. These tendencies were common throughout the entire experiment, with SeaWiFS output greater by up to 20% higher over clean skies and open water, becoming worse with higher aerosol optical depths. The difference in these AOD outputs is shown on the bottom left, showing low excess error from SeaWiFS in low dust environments, as expected.

The bottom left plot from Figure 18 is plotted again in Figure 18, this time in relative percentage difference above AVHRR instead of in absolute AOD amount. Anomalous high values south of Pyongyang (#1) are caused by turbidity, Vladivostok (#2) caused by dust and cloud edge.

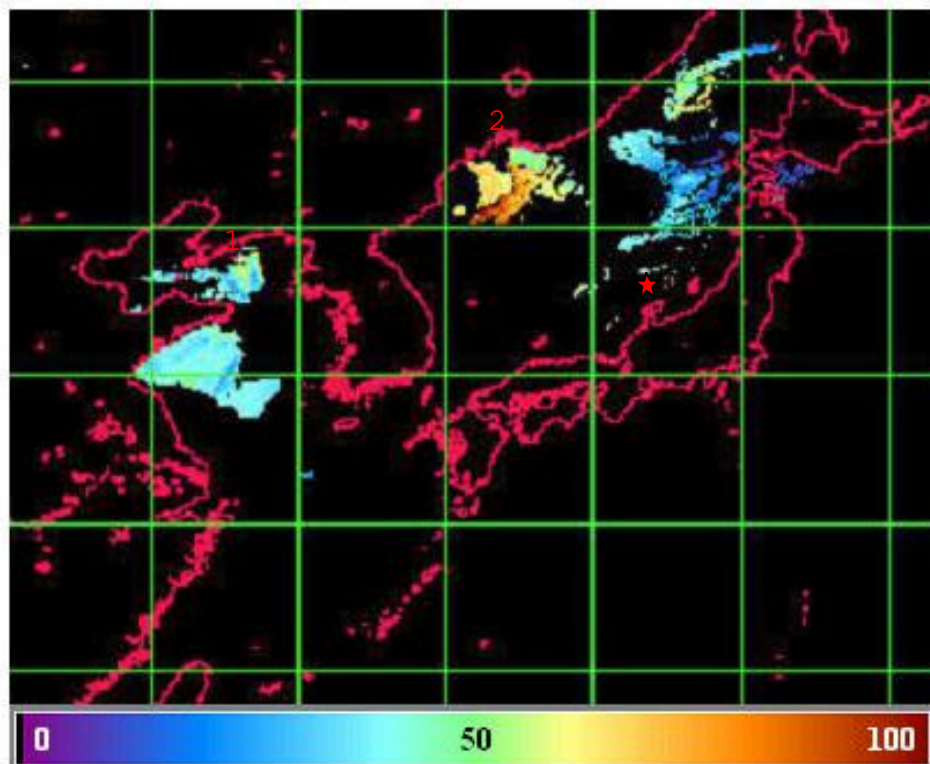


Figure 18. Percent difference between SeaWiFS and AVHRR AOD for April 25, 2001.

Refined parameters for Rayleigh scatter and ozone extinction reduced the excess SeaWiFS AOD values by 6% to 12%. Figure 19 shows the latest iteration of parameterization with AOD coefficients applied for this region of interest. The divisions are due to smoothing on the part of the algorithm: large gradients between adjacent pixels are mistaken by the computer as cloud edge, thus they are deleted from the image.

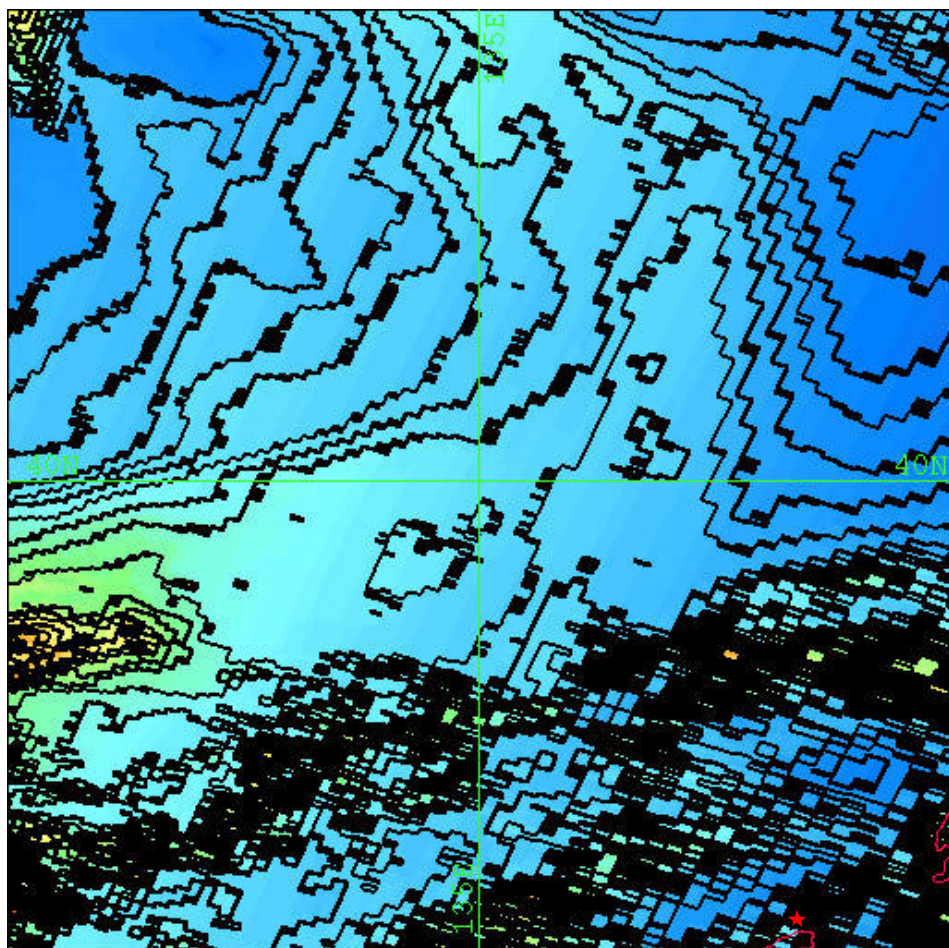


Figure 19. Latest iteration of NPS AOD algorithm for April 25, .2001

The SeaWiFS channel six value for this case is $5.6 \text{ W/m}^2 \text{ sr m}$, channel eight is $2.49 \text{ W/m}^2 \text{ sr m}$. The ratio of channels six and eight, known as S_{12} , is 1.59. The phase function therefore is 0.15 using a backscatter angle of 128° and size distribution model number 5.64. With total radiance of $60.18 \text{ W/m}^2 \text{ sr m}$, Rayleigh radiance removed as $19.45 \text{ W/m}^2 \text{ sr m}$, and the remaining aerosol radiance is $40.72 \text{ W/m}^2 \text{ sr m}$. Calculating Equation 6 gives an AOD of 0.49 for SeaWiFS. NOAA-16 channel one radiance value is $4.69 \text{ W/m}^2 \text{ sr m}$, channel two is $2.66 \text{ W/m}^2 \text{ sr m}$, for an S_{12} ratio of 1.34. For a total radiance of 21.59 , Rayleigh radiance 9.29 , the aerosol radiance is 10.51 for phase function look-up of 0.26. The output AOD is 0.44, having selected model number 1 with backscatter angle 157° .

A "light" dust day, AOD error was small in this case. The difference in retrieved AOD is small, even though the aerosol radiance values are quite different. This is caused by entering the S_{12} lookup tables at widely separated look angles and returning nearly identical phase functions from two different modal radius curves which balance each other in the end.

2. Similar Look Angle, Different AOD: Day 102.

This second event shows closely-spaced overhead passes near the same location to isolate the potential causes for differences in AOD output between the two sensors. The location of interest for this case is $33^\circ 15'$ North latitude, $126^\circ 54'$ East longitude. Cheju Island, is seen in Figures 20 & 21. Located south of Pusan, South Korea and

west of Sasebo and Nagasaki, Japan, the site was ideal in its central location and as a ground sunphotometer site. However, it had a unique impediment to AOD retrieval, as well. This was the first time during an ACE experiment that scientists encountered the well-known possibility of surface reflection by phytoplankton blooms.

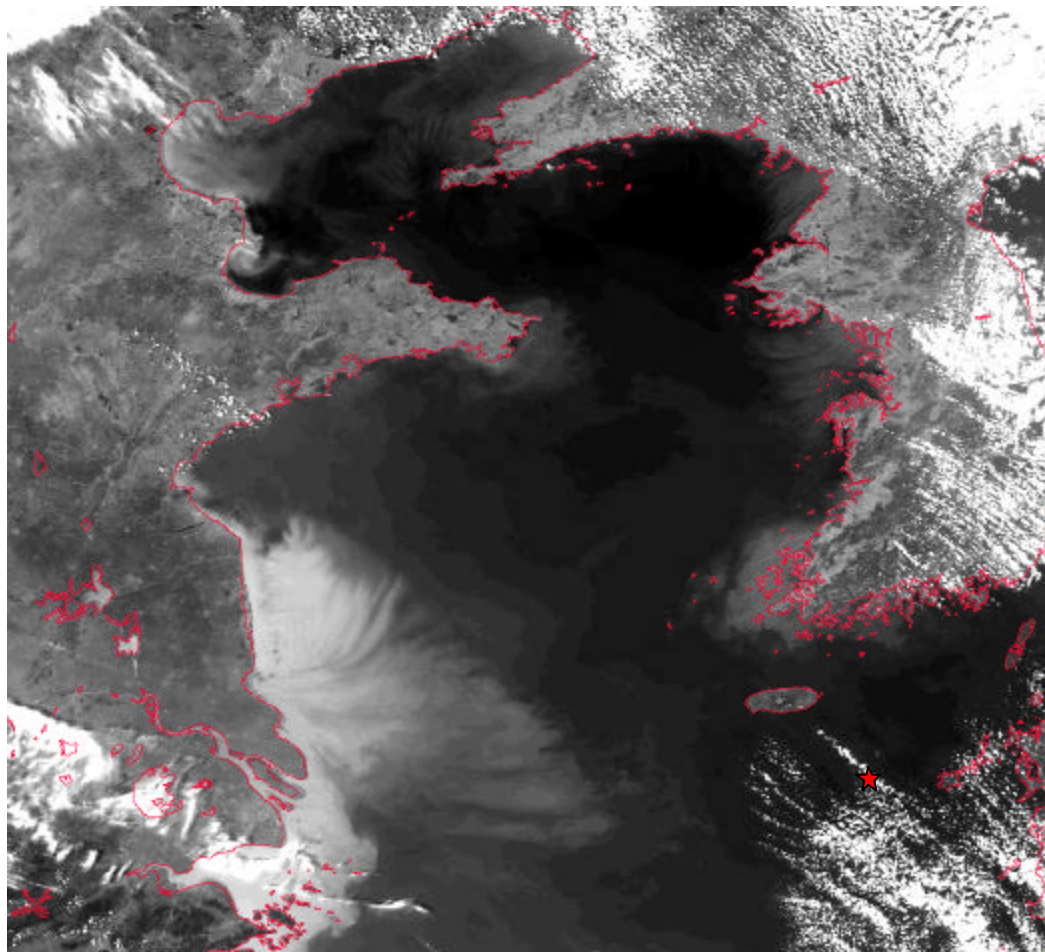


Figure 20.

NOAA-16 pass 20011020508Z, April 12, 2001.

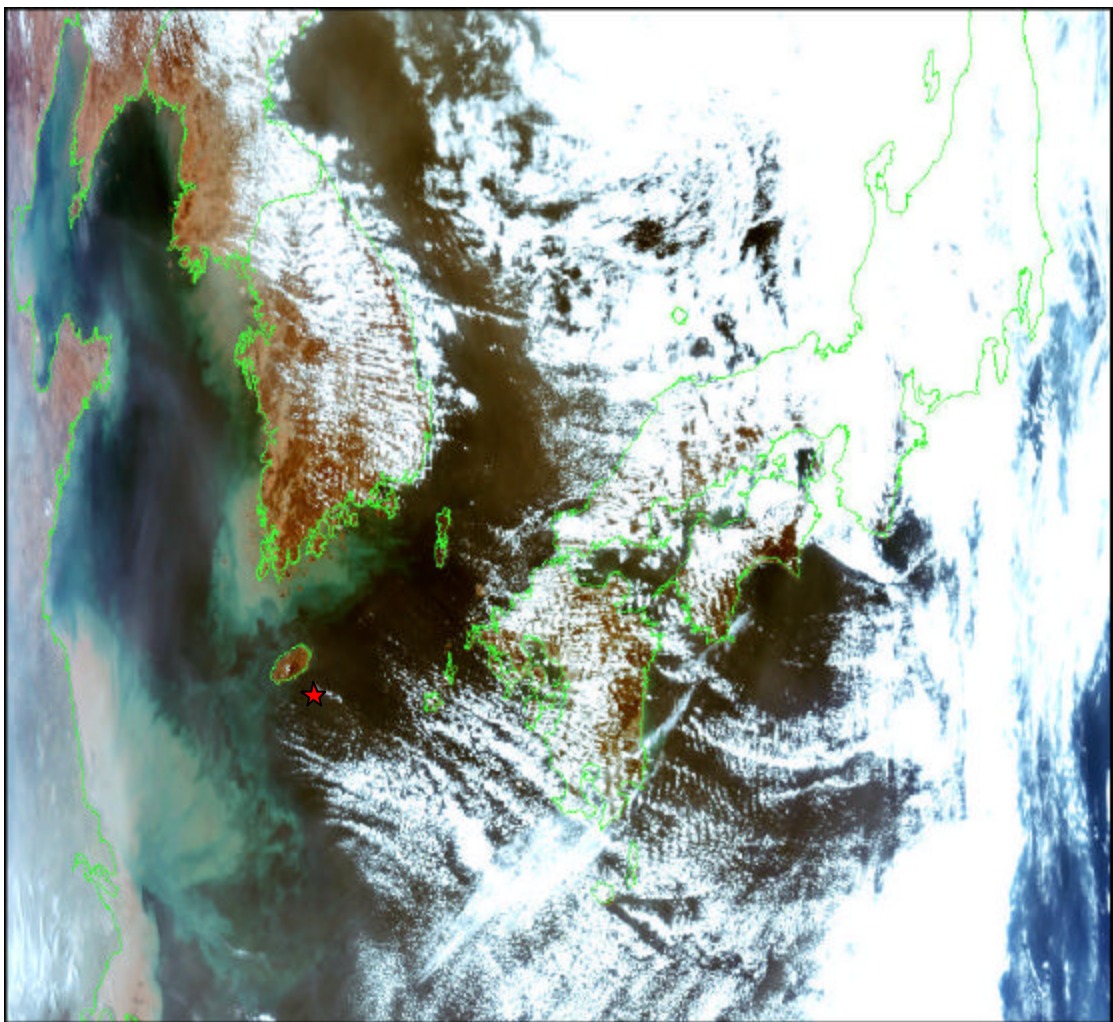


Figure 21. SeaWiFS pass 20011020333ZZ; April 12, 2001.

Red tides were seen to have been flowing from the Chinese coast to the southeast towards the Tsushima Straits (Figure 22). A yearlong deep flow is formed by the Yellow Sea Warm Current and the China Coastal Current. Flowing counter to the counter-clockwise gyre pattern might seem contrary to a physical oceanographer, but these blooms are quite shallow and drift at the will of the prevailing winds rather than ocean-basin thermohaline forcing.

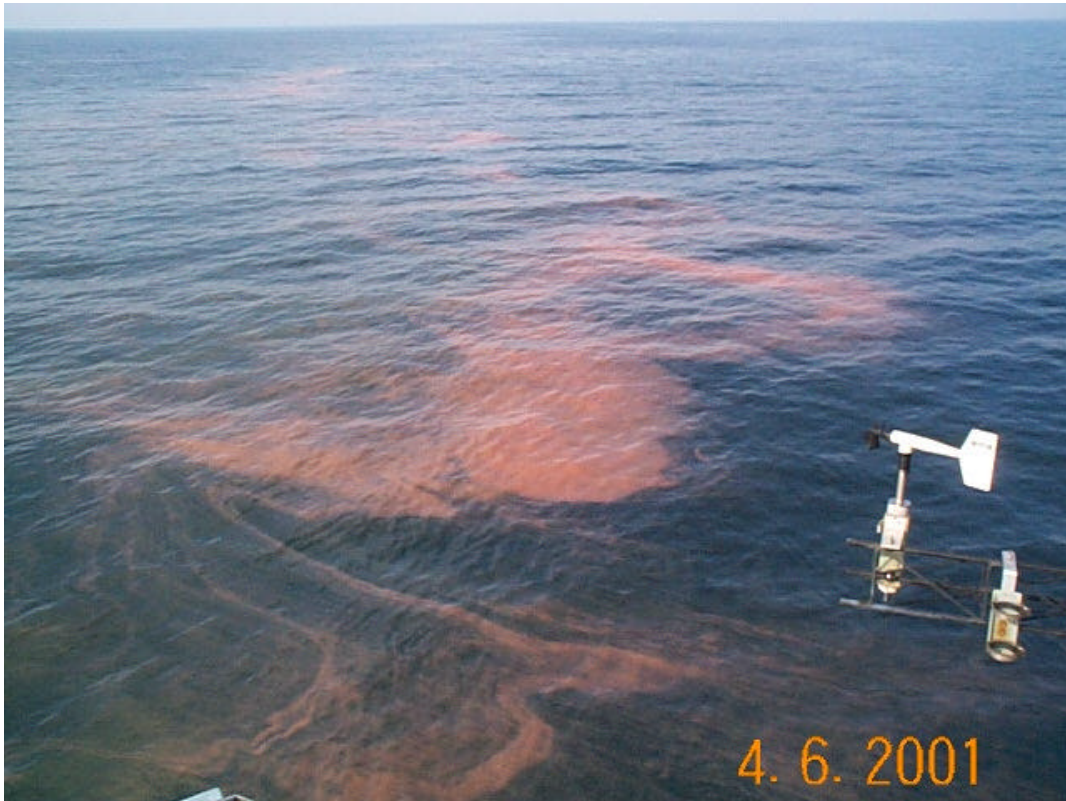


Figure 22. Red tides in the Yellow Sea from the R/V *Ron H. Brown*. (Photo courtesy of Piotr Flatau)

These red tides raise surface reflectance, especially at red visible wavelengths. Seawater absorbs the near-infrared wavelengths so well that it can generally be thought of as nonreflective in the absence of other materials. Phytoplankton pigment may create a greater effect in SeaWiFS channel six than AVHRR channel one due to its narrow bandwidth centered at 0.670 μm . Complications arise when blooms, oil slicks, foam whipped up by winds over 14 meters per second, and partially dissolved sediment are present. Regional studies in this area are hampered by the same conditions that give the Yellow Sea its name—up to 1.4 billion metric tons per year of sediment transport from the Yangtze River alone.

Red tides often bloom in 24-48 hours and last one week or longer, often dying out just as quickly due to lack of nutrients. Figure 23 shows an interesting three-day series over Cheju Island from April 12, 2001 to April 14, 2001.

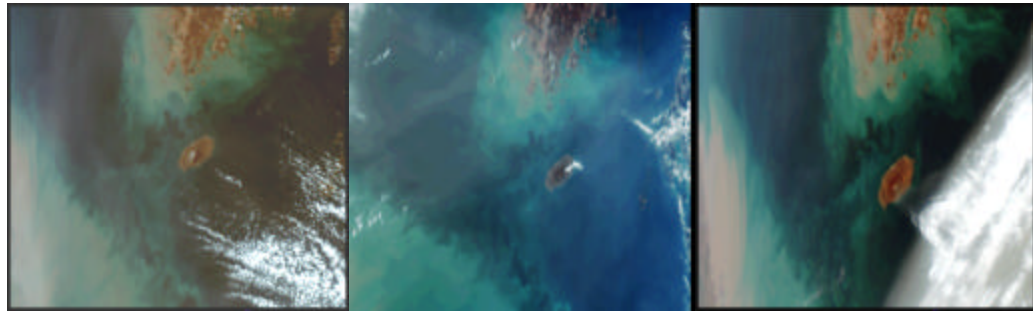


Figure 23. Red tides and coastal turbidity variation from space; April 12-14, 2001.

Image one shows the largest plankton blooms as well as aerosol flowing from north to south along the left edge of the image. Image two shows less plankton and an obvious wind shift from the southwest. Image three shows even less plankton but greater turbidity along the extreme left of the image. Decaying plankton change color (reflecting light at different wavelengths) from green or red to yellow and brown. Sample imagery from a three-day period show changes in underlying seawater constituents that could carelessly be taken for aerosol.

a. Weather at Nearest Aeronet Station

The winds over Cheju on April 12, 2001 were common over the entire experiment period. Seen in Figure 24, north-northwest winds vary in intensity and back from the west with the passage of numerous lows. These nearly always passed to the north with their associated cold fronts lingering a day or two behind. The Himalayan high has brought clear skies on this day and good conditions for AOD retrievals.

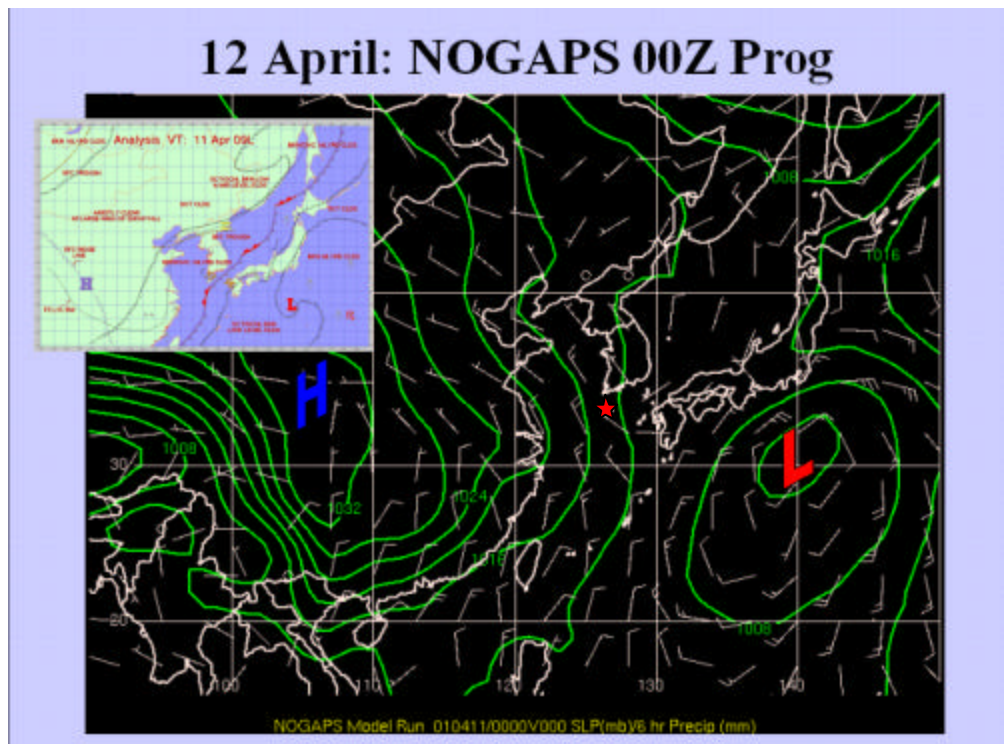


Figure 24.

Meteorological conditions for April 12, 2001.

b. NPS Model Output

Figure 25 is unique for the study in that they have exactly the same scattering angles, 162° . Higher dust values over the western Sea of Japan and Yellow Sea are observed. Initial SeaWiFS parameterization coefficients produced an AOD value of 0.66 (upper left); modifications brought this down to 0.58, a decrease of 12.1%. The AVHRR optical depth value (upper right) of 0.44 was 31.8% lower still. This excessive SeaWiFS optical depth at higher AODs was common.

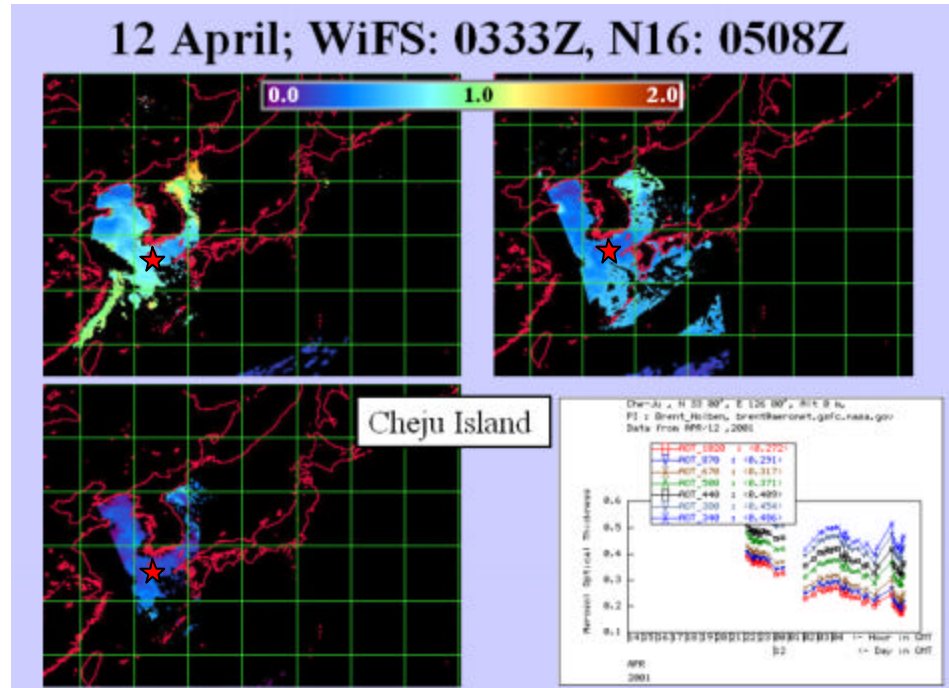


Figure 25. SeaWiFS AOD, NOAA-16 AOD, AOD difference, and Aeronet data for April 12, 2001.

Further complicating this retrieval were the underlying red tide filaments seen in the upper left of Figure 25, and more clearly as blotches in the center of

Figure 26. Compare this to the uniform difference values for the clean skies in case one.

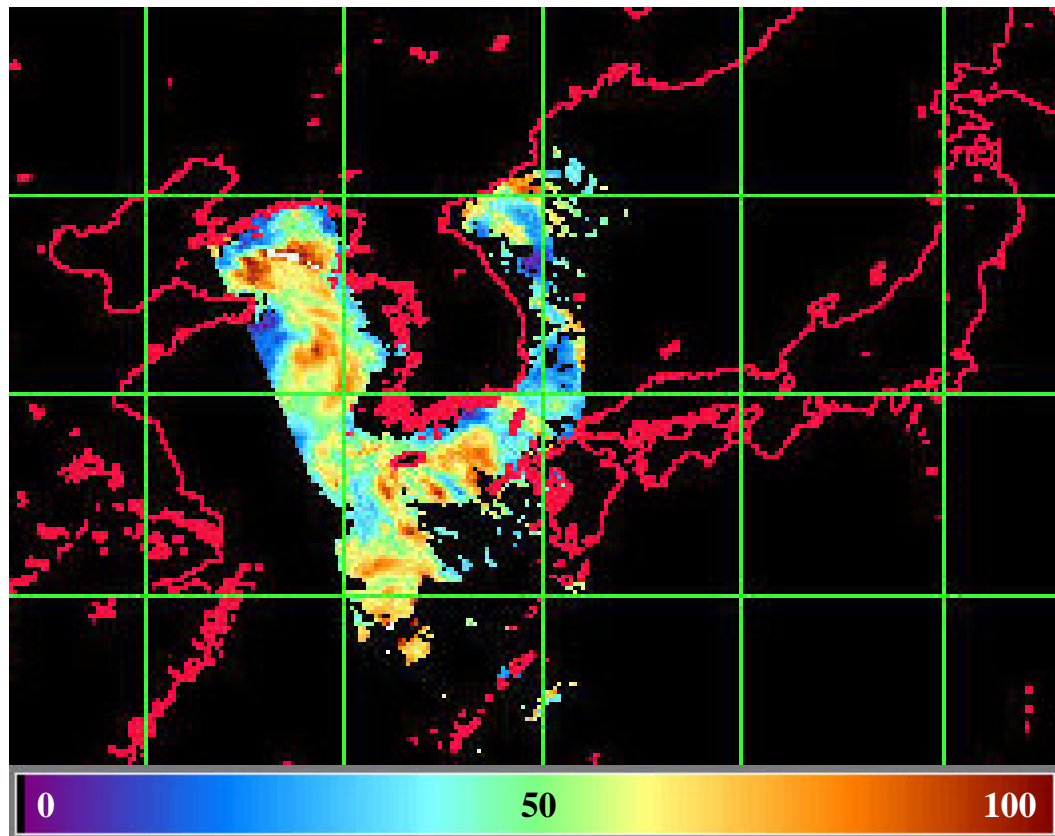


Figure 26. Percent difference between SeaWiFS and AVHRR AOD for April 12, 2001.

Differences in SeaWiFS and AVHRR AOD are clearly seen in the above Figure 27 over 28, after the improved Rayleigh and ozone coefficients have been applied.

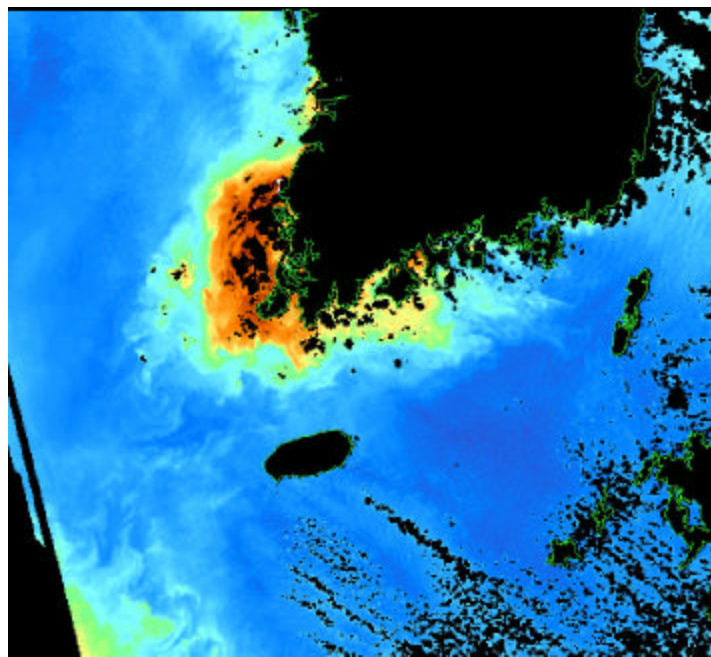


Figure 27.

NOAA-16 AOD product, April 12, 2001.

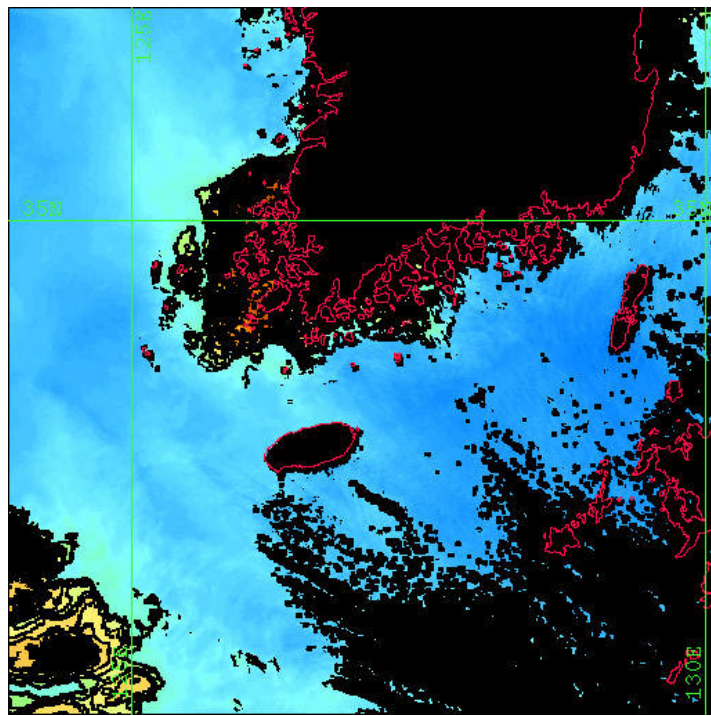


Figure 28.

Latest iteration of NPS AOD algorithm for
April 12,.2001

The SeaWiFS channel six value for this case is $2.42 \text{ W/m}^2 \text{ sr m}$, channel eight is $0.95 \text{ W/m}^2 \text{ sr m}$. The ratio of channels six and eight, S_{12} , is 1.66. The phase function thus is 0.18 using a backscatter angle of 162° and size distribution model number 6.51. With total radiance of only 24.94 this time, Rayleigh radiance at 8.53, and the remaining aerosol radiance 16.41. AOD becomes 0.58 for SeaWiFS. NOAA-16 channel one radiance value is $4.57 \text{ W/m}^2 \text{ sr m}$, channel two is $2.72 \text{ W/m}^2 \text{ sr m}$, for an S_{12} ratio of 1.27. For a total radiance 21.08, Rayleigh radiance 8.38, the aerosol radiance is 10.90 for phase function look-up of 0.28. The output AOD is 0.44, again with model number 1, backscatter angle also 162° . SeaWiFS error is greater as AOD increases, however the increased surface reflection contamination probably has the greatest effect on AOD error in this region.

3. Extremely high AOD event: Day 100.

Compare the preceding low AOD values to a particularly dirty event on Julian day 100 shown in Figures 29 and 30.



Figure 29.

NOAA-16 pass 20011000349Z; April 10, 2001.

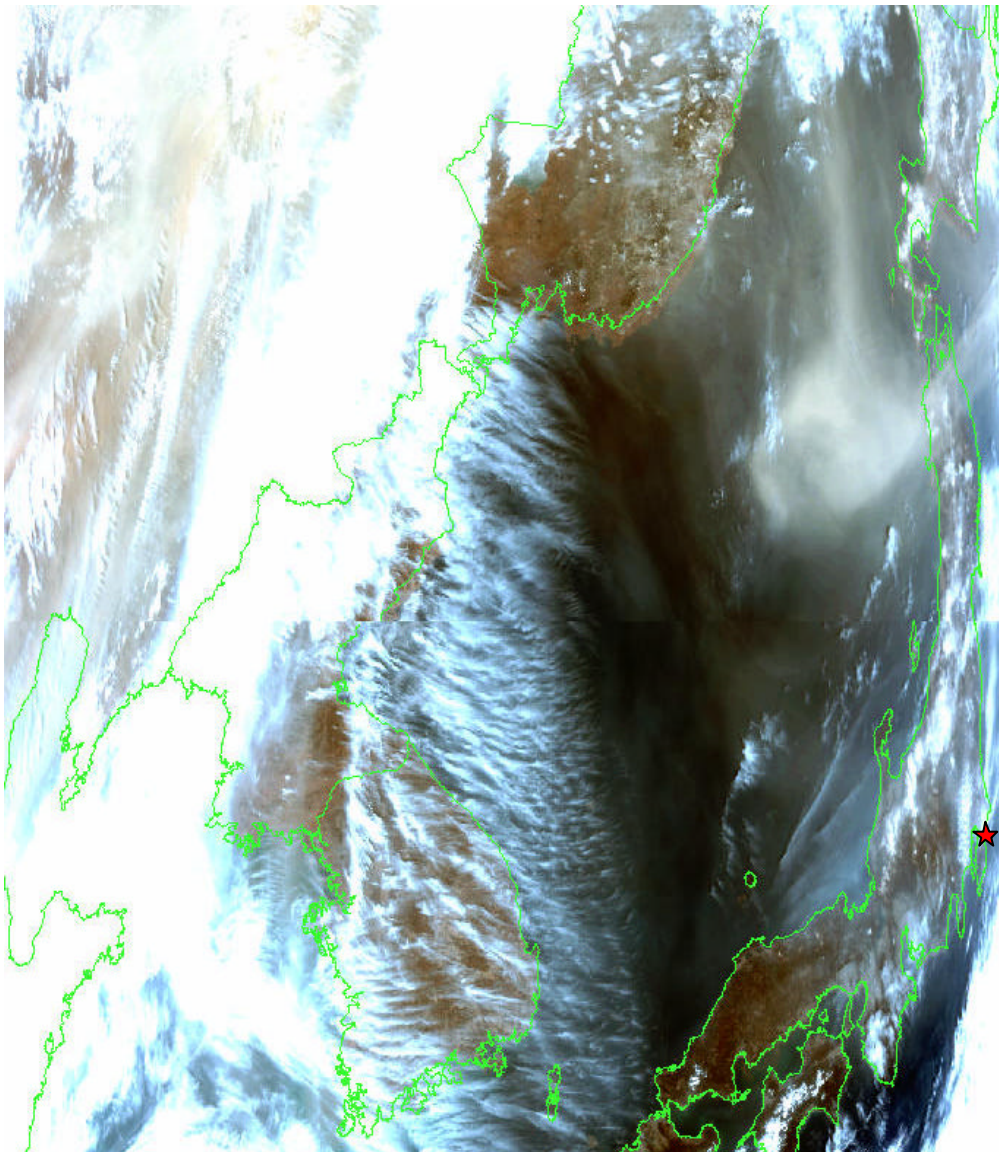


Figure 30. SeaWiFS pass 20011000345Z; April 10, 2001.

The location of comparison in this case ($37^{\circ} 32' N$, $141^{\circ} 18' E$), is off the eastern coast of Honshu northeast of Tokyo Bay. The majority of the dust plume lags behind a frontal passage over Japan, with a narrow leader of dust to the east. Further zooming in these images shows cloud shadow on the underlying dust plume, fixing its altitude between the marine boundary layer and the cloudbase. A

glitch in the image downlink can be seen in Figure 30 through North Korea.

a. Weather at Nearest Aeronet Station

Upper-level westerlies carried the aerosol to the east across Japan above the NOGAPS surface wind fields in Figure 31.

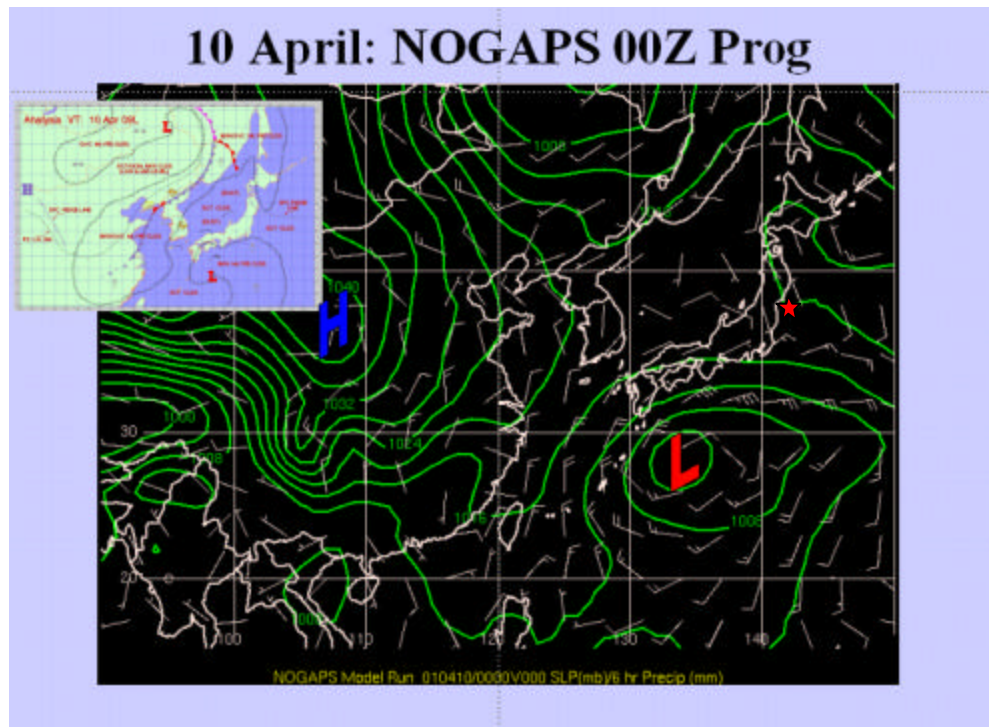


Figure 31.

Meteorological conditions for April 10, 2001.

b. NPS Model Output

Aerosol optical depths in Figure 32 have been clipped at 2.0, but actually exceeded 4.5. The AOD output was lost when it began merging with clouds associated with a low forming northeast of Vladivostok.

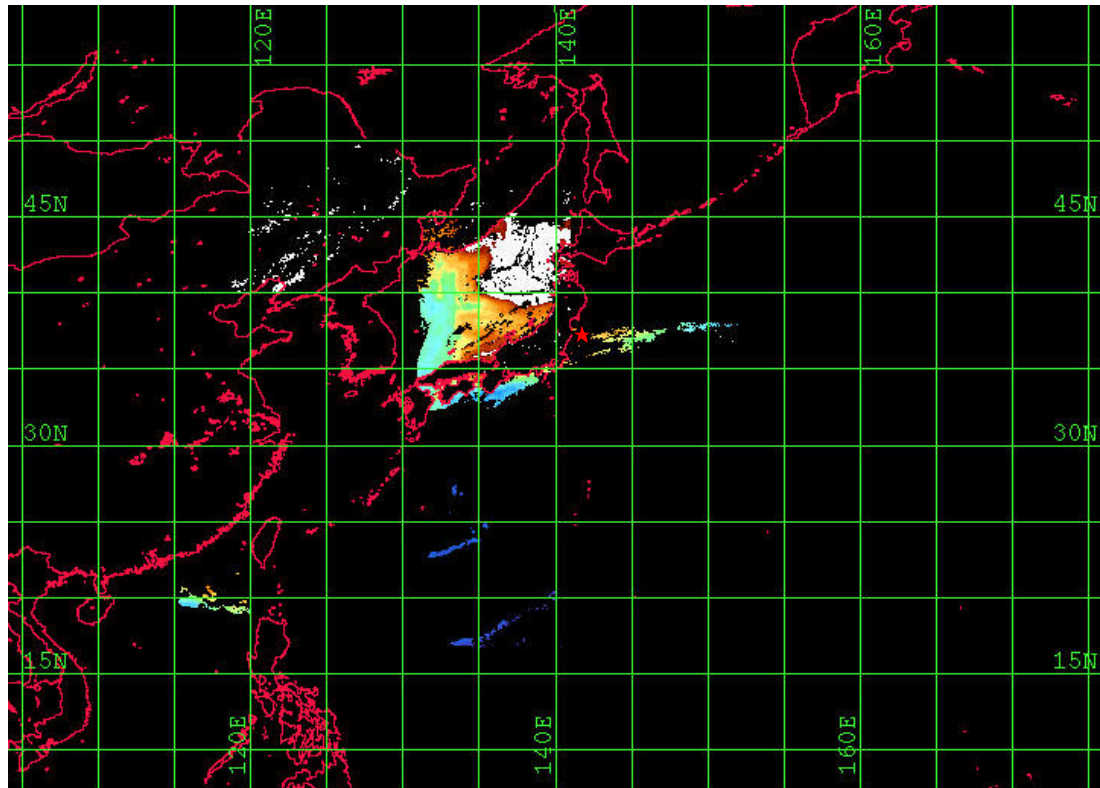


Figure 32. SeaWiFS AOD 20011000345Z; April 10, 2001.

This very dirty case SeaWiFS channel six value is $6.05 \text{ W/m}^2 \text{ sr m}$, channel eight is $2.91 \text{ W/m}^2 \text{ sr m}$. S_{12} is 1.73. The phase function is 0.14 using a backscatter angle of 130° and size distribution model number 6.26. With total radiance as 66.32, Rayleigh radiance removed as 10.88, the remaining aerosol radiance is now as high as 55.44. Equation 6 gives a high AOD of 1.47 for SeaWiFS. NOAA-16 channel one radiance value is $6.33 \text{ W/m}^2 \text{ sr m}$, channel two is

4.33 W/m² sr m, for an S₁₂ ratio of 1.27. For a total radiance 28.13, Rayleigh radiance 6.67, the aerosol radiance is 19.78 for phase function look-up of 0.23. The AOD output is only 0.799, having selected low model number one and backscatter angle at the phase function curve inflection point near 142°. SeaWiFS error appears to increase nonlinearly as AODS continue to rise. Multiple scatter in the air column would explain this AOD retrieval output. As the number of Mie scatter particles in a given atmospheric volume increases, the chance of repeated scatter towards the sensor rises. This in turn increases the total radiance observed, leading to excessive AOD output.

D. VALIDATION

The NPS model with SeaWiFS input showed some skill at measuring aerosol optical depth compared to AVHRR and Aeronet sunphotometer. Iterations of the corrected validation process will continue to improve the Rayleigh and ozone parameterization. Table 1 shows the latest values used in this thesis.

Table 1. Corrected parameterization for NPS SeaWiFS AOD algorithm.

N-16:	Ch. 1	Ch. 2	WiFS:	Ch. 6	Ch. 8
ρ_s	0.005	0	ρ_s	0.005	0
E _o	1628	1030	E _o	1584	1030
δ_R	0.057	0.019	δ_R	0.044	0.019
δ_{O_3}	0.027	0.002	δ_{O_3}	0.013	0.002

Figure 33 shows an initial scatter plot of the 27 matching SeaWiFS and AVHRR overpasses prior to selecting the three critical events. It was assumed that SeaWiFS AODs would be a linear factor higher than AVHRR. Simple parameterization corrections could then be used to lower the linear best-fit AOD distribution to match Aeronet and AVHRR AOD values.

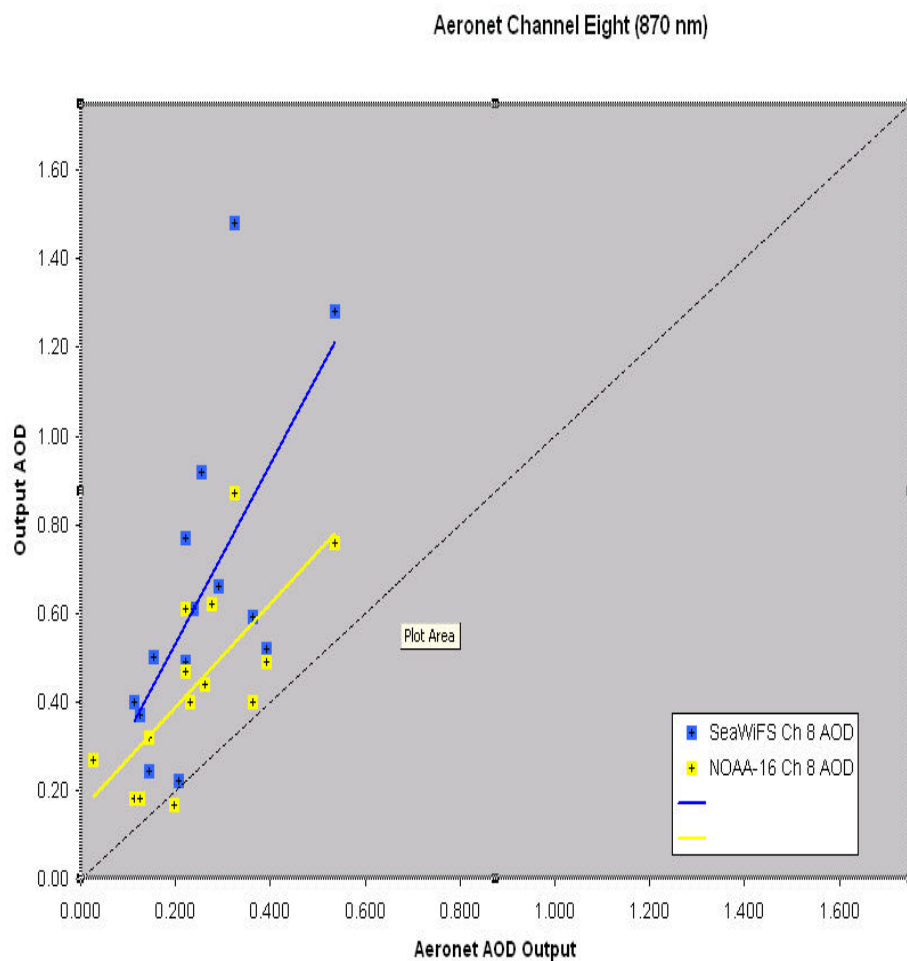


Figure 33. Initial summary of SeaWiFS and NOAA-16 AOD compared to Aeronet ground Observation at 870 nm, with linear best-fit superimposed.

Figures 34 & 35 show improved parameterization AOD (green circles) plotted under initial SeaWiFS AOD values (blue squares) against Aeronet channel six and channel eight AOD. Only five of the cases with Aeronet data available from the original 27 matches are plotted for clarity. Taiwan (triangles) was consistently plankton bloom-free and dust-free and had the lowest error of any matching comparison and negligible change due to improved parameterization.

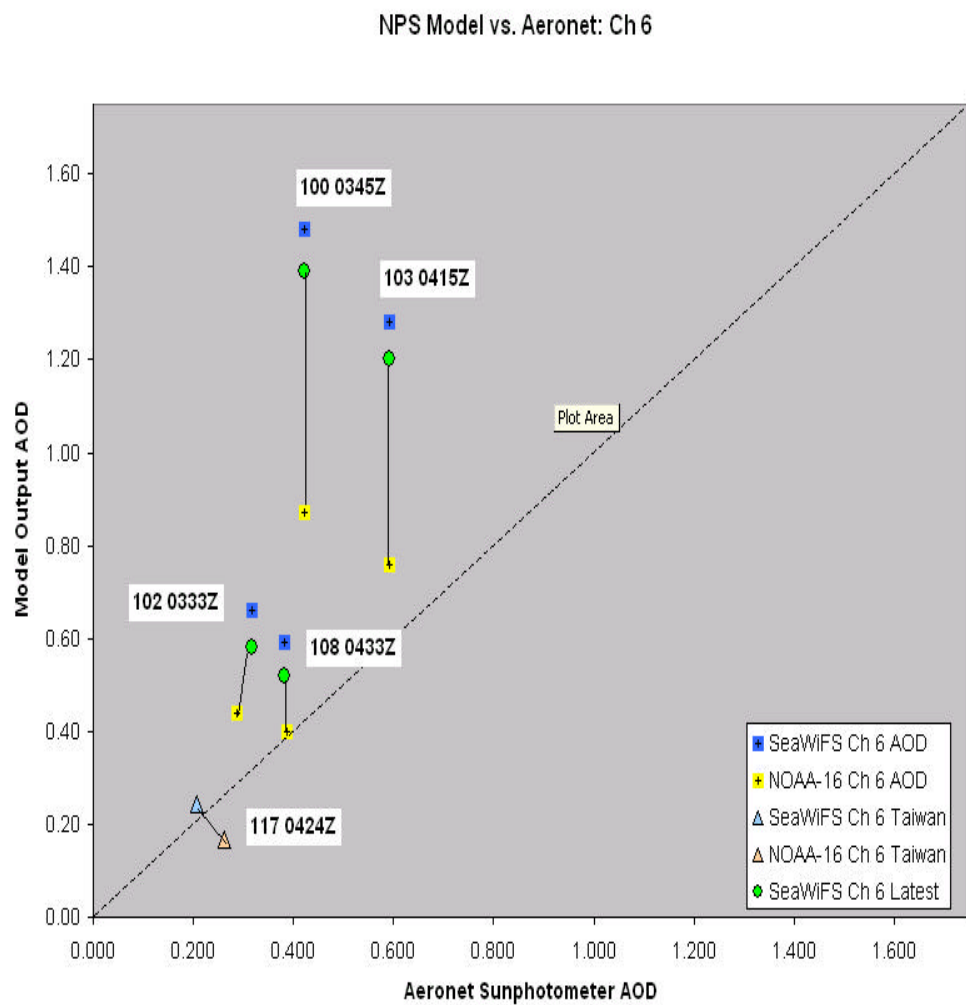


Figure 34. SeaWiFS AOD comparison with Aeronet ground observations at 670 nm.

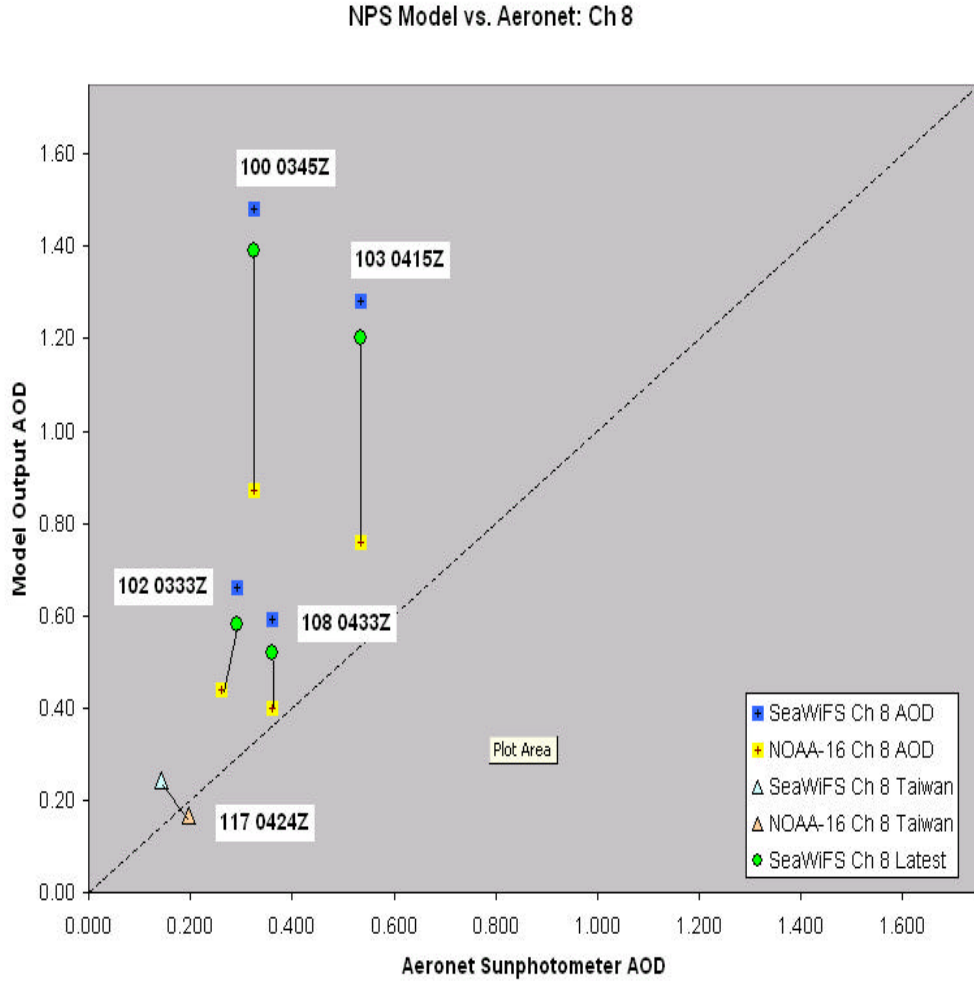


Figure 35.

SeaWiFS AOD comparison with Aeronet ground observations at 870 nm.

SeaWiFS error does not appear to be linear with increasing AOD under the spherical aerosol, single-scatter assumption.

Table 2 lists columns of: SeaWiFS and AVHRR overpass time, elapsed time separation, nearest Aeronet Station, channel six and eight Aeronet AOD for overpass time, SeaWiFS and AVHRR AODS, latest parameterization SeaWiFS AOD, and relative decrease in AOD error from AVHRR.

Table 2. Reduction in SeaWiFS AOD error with improved parameterization.

<u>WiFS</u>	<u>N-16</u>	<u>dT</u>	<u>Aero</u>	<u>AW6</u>	<u>AN6</u>	<u>AW8</u>	<u>AN8</u>	<u>W1</u>	<u>N1</u>	<u>AOD</u>	<u>Drop</u>
100 0345	100 0349	-4	Noto	0.421	0.421	0.324	0.324	1.48	0.87	1.39	6.08%
102 0333	102 0508	95	Cheju	0.316	0.287	0.291	0.262	0.66	0.44	0.58	12.12%
103 0415	103 0457	42	Cheju	0.592	0.592	0.535	0.535	1.28	0.76	1.20	6.25%
108 0433	108 0405	-28	Cheju	0.383	0.386	0.362	0.362	0.59	0.40	0.52	11.86%
115 0433	115 0433	0	-	-	-	-	-	0.50	0.44	0.46	8.00%

THIS PAGE INTENTIONALLY LEFT BLANK

V. CONCUSIONS & RECOMMENDATIONS

A critical analysis of the modification to the NPS aerosol optical depth retrieval model for SeaWiFS input shows promising potential with a few shortcomings. SeaWiFS AOD values were higher by 20-50%, in a non-linear manner at high AOD. Future construction of a multi-dimensional S_{12} lookup table for multiple scatter may be required to correct this error.

Size distribution model numbers were larger in all cases, as well as S_{12} ratios. Aerosol radiance for case one was four times higher for SeaWiFS and 50.6% greater for case two. These factors, along with backscatter phase angle, determine the phase function intrinsic to aerosol optical depth from equation six.

Red tides combined with highly reflective turbid seawater complicates the AOD retrieval process. Had the ship *Ron Brown* been able to gather more *in-situ* upward-looking radiance measurements and collect some of the phytoplankton for chemical analysis, it might be possible to screen its reflective bandwidths in the future. The interrelated light-reflecting properties of aerosol and ocean sediment continue to plague researchers and the warfighter interested in maritime safety during mine-clearing operations. For further discussion on turbidity retrievals and its effects on remote sensing during the same ACE-Asia experiment, see Rocha (2001).

The results of this study of NPS AOD model modification merely builds upon the foundation lain by Brown, 1997 and Smith, 1998. Further steps will surely

incorporate improved sensor technology such as MODIS aboard the TERRA satellite or the future NPOESS.

Further areas to explore in regards to this study include:

- Improved model integration for vertical lifting and surface type for dust source region, relative humidity and subsidence for aerosol growth and water deposition (radius change) and precipitation from the air column over time.
- Improved cloud mask ability in the lack of infrared split-channel techniques.
- Improved plankton bloom detection and testing the purely single-scatter, specular reflection, spherical particle assumptions.
- Ground-truth data collection was hampered in this experiment due to political constraints. Had the ship *Ron Brown* or the C-130 and King Air been able to spend more time in the Yellow Sea, a more complete knowledge of the aerosol constituents would be known. Definitive data on the size and chemical makeup of this dust leaving the Chinese coast would have allowed for further model validation. The parameterization of the phase function remains a largest error source and the greatest uncertainty for AOD algorithms. In the lack of *in-situ* measurements, future improvements to tools such as the NASA/Goddard Space Flight Center MODIS dust classification look promising.

- Add data sets to this experimental series by measuring AOD along with plankton bloom-prone regions navigable for US research vessels, including the southern California coast and the Gulf of Mexico as substitutes for the Yellow Sea and Bohai Bay. Currently, good results have been achieved in the vicinity of Taiwan; further study into the South China Sea and the South Pacific is warranted.

THIS PAGE INTENTIONALLY LEFT BLANK

LIST OF REFERENCES

- ACE-ASIA, (1999). Project Prospectus. <http://saga.pmel.noaa.gov/aceasia/prospectus2000/>.
- Atmospheric Radiation Measurement Program, (2002). Cimel Sunphotometer (CSPOT). <http://www.arm.gov/instruments/Static/cspot.html>.
- Bates, T. S., P. K. Quinn, D. S. Covert, D. J. Coffman, J. E. Johnson, and A. Weidenohler (1999) Aerosol physical properties and processes in the lower marine boundary layer: a comparison of shipboard sub-micron data from ACE-1 and ACE-2. *Tellus*, **52B**, 258-272.
- Brown, B. B. (1997). Remote measurement of aerosol using the NOAA POES AVHRR and GOES Imager during TARFOX. M.S. Thesis, Naval Postgraduate School, Monterey, CA, 67pp.
- Durkee, P. A., F. Pfiel, E. Frost and R. Shema (1991). Global analysis of aerosol particle characteristics. *Atmos. Env.*, **25A**, 2457-2471.
- Durkee, P. A., K. E. Nielsen, P. J. Smith, P. B. Russell, B. Schmid, J. M. Livingston, B. N. Holben, C. Tomasi, V. Vitale, D. Collins, R. C. Flagan, J. H. Seinfeld, K. J. Noone, E. Ostrom, S. Gasso, D. Hegg, L. M. Russell, T. S. Bates, and P. K. Quinn, (1999). Regional aerosol optical depth characteristics from satellite observations: ACE-1, TARFOX, and ACE-2 results. *Tellus*, **52B**, 484-497.
- Gordon, H. R. and D. K. Clark (1980). Atmospheric effects in the remote sensing of phytoplankton pigments. *Boundary Layer Met.*, **18**, 300-313.
- Kidder, S. Q. and T. H. Vonder Haar (1995). Satellite Meteorology, An Introduction. Academic Press, San Diego.
- Kidwell, K. B. (1995). NOAA polar orbiter data users guide. National Environmental Satellite, Data, and Information Service (NESDIS), National Oceanic and Atmospheric Administration, 394pp.

- Liou, K. N. (1980). An Introduction to Atmospheric Radiation. Academic Press, New York.
- Hooker, S. B., E. R. Firestone and J. G. Acker, Eds. (1999). *SeaWiFS Prelaunch Radiometric Calibration and Spectral Characterization*. NASA/Goddard Space Flight Center SeaWiFS Project Technical Report Series, Technical Memorandum 104566, Volume 23.
- Hooker, S. B., E. R. Firestone and J. G. Acker, Eds. (1999). *Ocean Optics Protocols for SeaWiFS Validation, Revision 1*. NASA/Goddard Space Flight Center SeaWiFS Project Technical Report Series, Technical Memorandum 104566, Volume 25.
- Hooker, S. B., and E. R. Firestone, Eds. (2000). *SeaWiFS Postlaunch Calibration and Validation Analyses, Part 1*. NASA/Goddard Space Flight Center SeaWiFS Project Technical Report Series, Technical Memorandum 2000-206892, Volume 9.
- Hooker, S. B., and E. R. Firestone, Eds. (2000). *SeaWiFS Postlaunch Calibration and Validation Analyses, Part 2*. NASA/Goddard Space Flight Center SeaWiFS Project Technical Report Series, Technical Memorandum 2000-206892, Volume 10.
- Quinn, P. K., T. S. Bates, D. J. Coffman, T. L. Miller, J. E. Johnson, D. S. Covert, J.-P. Putaud, C. Neusub, and T. Novakov. (1999) A comparison of aerosol chemical and optical properties from the first and second Aerosol Characterization Experiments. *Tellus*, **52B**, 239-257.
- Rocha, J. D. (2001). SeaWiFS analysis of the Japan and East China Sea air/sea environment. M.S. Thesis, Naval Postgraduate School, Monterey, CA, 61pp.
- Saunders, R. W. and K. T. Kriebel (1988) An improved method for detecting clear sky and cloudy radiation from AVHRR data. *Int. J. Rem. Sen.*, **9**, 123-150.
- Schmid, B., J. M. Livingston, P. B. Russell, P. A. Durkee, H. H. Jonsson, D. R. Collins, R. C. Flagan, J. H. Seinfeld, S. Gasso, D. A. Hegg, E. Ostrom, K. J.

Noone, E. J. Welton, K. J. Voss, H. R. Gordon, P. Formenti, and M. O. Andrea, (1999). Clear-sky closure studies of the lower tropospheric aerosol and water vapor during ACE-2 using airborne sunphotometer, airborne in-situ, space-borne, and ground-based measurements. *Tellus*, **52B**, 568-593.

Sokolik, I. N. and O. B. Toon, (2002). Incorporation of mineralogical composition into models of the radiative properties of mineral aerosol from UV to IR wavelengths. *J. Geo. Res.*, in press.

Xu, J. and M. Bergin, (2001). Aerosol optical properties and direct radiative forcing at Yulin, China.
http://www.ce.gatech.edu/~mhbergin/aceasia_yulin.pdf

THIS PAGE INTENTIONALLY LEFT BLANK

INITIAL DISTRIBUTION LIST

1. Defense Technical Information Center
Ft. Belvoir, Virginia
2. Dudley Knox Library
Naval Postgraduate School
Monterey, California
3. CDR James A. Hill
Naval Postgraduate School
Monterey, CA
4. Chairperson, Department of Oceanography
Naval Postgraduate School
Monterey, CA
5. Chairperson, Department of Meteorology
Naval Postgraduate School
Monterey, CA
6. Professor Philip A. Durkee, MR/De
Naval Postgraduate School
Monterey, CA
7. Professor Kenneth L. Davidson, OC/De
Naval Postgraduate School
Monterey, CA